Research Square

Preprints are preliminary reports that have not undergone peer review.
They should not be considered conclusive, used to inform clinical practice,
or referenced by the media as validated information.

Nonlinear primary resonance of doubly curved laminated nanocomposite shells within shear deformation theory

Mahmure Avey
İstanbul Gelişim Üniversitesi
Salim Yüce
sayuce@yildiz.edu.tr

Yıldız Technical University

Research Article

Keywords: Doubly curved surfaces, laminated nanocomposites, primary resonance, elastic foundation, nonlinearity, multi-time-scale methods, shear deformation theory

Posted Date: November 2nd, 2026

DOI: https://doi.org/10.21203/rs.3.rs-11269763/v1

License: This work is licensed under a Creative Commons Attribution 4.0 International License.
Read Full License

Additional Declarations: No competing interests reported.

Nonlinear primary resonance of doubly curved laminated nanocomposite shells within shear deformation theory

MAHMURE AVEY[a,b], SALIM YÜCE[*c]

[a]Department of Computer Programming, Istanbul Gelisim University, 34310 Avcilar, Istanbul, Türkiye, E-mail: mavey@gelisim.edu.tr and mahmureavey@gmail.com

[b] Department of Mathematics of Yıldız Technical University Davutpaşa Campus, 34220 Esenler, Istanbul, Türkiye

[c*]Department of Mathematics, Faculty of Arts and Sciences Yıldız Technical University Davutpaşa Campus, 34220 Esenler, Istanbul, Türkiye

CORRESPONDENCE:

Prof. Dr. Salim Yüce

Department of Mathematics, Faculty of Arts and Sciences Yıldız Technical University Davutpaşa Campus, 34220 Esenler, Istanbul, Türkiye

E-mail: sayuce@yildiz.edu.tr and mahmureavey@gelisim.edu.tr

Abstract

Accurate prediction of nonlinear resonance in lightweight doubly curved composite structures is essential for ensuring their dynamic reliability under external excitations. This study develops a unified analytical framework for investigating the geometrically nonlinear forced vibration response of laminated functionally graded nanocomposite (FG-NC) shells with spherical and hyperbolic paraboloidal geometries supported by a Winkler elastic foundation (WEF). The structural formulation is established within shear deformation theory, while the nonlinear strain–displacement relations associated with the non-zero Gaussian curvature are explicitly retained to capture the curvature-induced nonlinear coupling mechanisms. The model simultaneously accounts for the through-thickness distribution and stacking sequence of the FG-NC layers, foundation–structure interaction, viscous damping, and harmonic excitation. The coupled nonlinear partial differential equations governing shell dynamics are transformed into a reduced-order nonlinear modal equation using the Galerkin procedure. The method of multiple time scales is subsequently employed to derive the modulation equations and closed-form amplitude–frequency response relations governing the primary resonance regime. The resulting analytical model provides an efficient means of identifying amplitude-dependent resonance shifts and quantifying the combined effects of geometric curvature, shear deformation, elastic foundation stiffness, excitation intensity, material distribution pattern, and laminate configuration on the nonlinear dynamic response. Extensive parametric investigations reveal the physical mechanisms through which these parameters alter the resonance characteristics and vibration amplitudes of spherical and hyperbolic paraboloidal FG-NC shells. The proposed framework therefore provides a computationally efficient reduced-order tool for the dynamic assessment and resonance-oriented design of advanced curved nanocomposite structures.

Keywords: Doubly curved surfaces; laminated nanocomposites; primary resonance; elastic foundation; nonlinearity; multi-time-scale methods; shear deformation theory

1. Introduction

Doubly curved shells constitute an important class of structural systems due to their high load-carrying capacity, geometric efficiency, and complex dynamic response. Their inherent curvature produces a strong interaction among membrane deformation, bending, and transverse shear effects, making their vibration and stability behavior highly sensitive to geometric and material parameters. Consequently, the development of mechanically consistent theories for predicting the nonlinear response of such structures has remained a fundamental objective in shell mechanics. The systematic study of geometric nonlinear vibration and stability problems in the literature began with the work of Donnell [1] and has since been enriched by the contributions of Ambartsumyan [2], Volmir [3], Reddy [4], Awrejcewicz [5], and Amabili [6], encompassing both classical and shear deformation theories. Developed under the assumptions of small strains and large displacements, these theories have provided powerful frameworks for explaining resonance, amplitude-dependent frequency shifts, dynamic instability, and post-buckling behavior in thin curved structures. Shear deformation theories, developed to accurately model transverse shear effects that cannot be neglected in thick and moderately thick shells, have significantly improved the accuracy of nonlinear vibration and stability analyses and enabled the construction of more realistic mechanical models. Nonlinear vibration characteristics, including amplitude-dependent frequency relationships and resonance curves, have demonstrated that shells are highly sensitive structures not only from a static perspective but also from a dynamic standpoint. In this context, both classical and contemporary studies indicate that the nonlinear dynamics of shells remains an important research area for mathematical modeling and advanced engineering applications [1–6].

The increasing demand for lightweight, high-performance structural systems has accelerated the development of nanocomposite materials with improved mechanical properties. Carbon nanotube (CNT) reinforced polymers stand out as one of the most promising classes of nanocomposite materials, combining low weight with exceptional rigidity and strength. Thanks to their nanoscopic geometries and superior material properties, CNTs can significantly improve the load-carrying capacity and dynamic behavior of composite structures [7]. Therefore, CNT-reinforced nanocomposites or FG-NCs are widely used in the analysis and design of advanced shell and plate systems where structural efficiency, vibration control, and durability are critical. Numerous studies have shown that even small amounts of CNT additions provide significant improvements in structural performance, making these materials an attractive alternative to conventional layered composites [8–13]. Following these studies, FG-NCs, where the material distribution can be designed according to structural performance requirements, have become an important research topic in the development of advanced single-layer shell structures. The ability to apply CNT reinforcement at different ratios throughout the thickness allows for the effective improvement of the mechanical behavior of functionally graded shell systems operating under dynamic loads. Therefore, numerous studies have been conducted on the vibration and stability problems of single-layer FG-NC shells under various

operating conditions, including elastic media. Research in literature has investigated the free and forced vibration behavior of structures with different shell geometries; and has evaluated in detail the effects of CNT volume ratio, distribution model, environmental effects, and structural parameters on the system response in the presence and absence of an elastic medium. The results obtained have shown that, in addition to the effects of the elastic medium, the degree of curvature and geometric nonlinear deformations are among the fundamental factors determining the dynamic response, and that neglecting these effects can lead to significant errors in engineering designs [14–24].

The investigation of forced vibrations in engineering structures has advanced considerably thanks to classical studies in the field of nonlinear dynamics and vibration theory [25, 26]. These studies have provided a fundamental infrastructure for evaluating complex dynamic responses and identifying critical phenomena such as resonance, instability and nonlinear frequency shifts that occur under external excitations.

In recent years, the dynamic behavior of advanced nanocomposite shell structures has attracted significant attention from researchers, resulting in a substantial increase in the number of studies on multilayer shell systems when birefringence and continuous medium effects are disregarded. Particular emphasis has been placed on nonlinear effects occurring during large amplitude vibrations, demonstrating that under these conditions, the structural response is strongly dependent on the vibration amplitude and external excitation characteristics [27–31]. As highlighted in the previous paragraph, in engineering applications, shell structures often operate not in a free environment, but on surrounding environments or elastic soils that provide additional support and rigidity [32]. Therefore, the mechanical interaction between the layered shell and the supporting medium plays a crucial role in determining the dynamic behavior of the system. There are a few studies in the literature that partially demonstrate that soil parameters can significantly alter vibration characteristics, influence the location of resonance regions, and increase the effective rigidity of the structure. The findings from these studies show that soil effects must be considered in the nonlinear dynamic analysis of laminated FG-NC shells [33–39]. Nevertheless, there are significant research gaps in the current literature regarding the comprehensive and systematic investigation of the nonlinear dynamical behavior of layered FG-NC shells with different curvature characteristics underground influence within SDT.

In this study, in order to address this gap, the geometric nonlinear forced vibration behavior of doubly curvature (spherical and hyperbolic paraboloid) laminated FG-NC shallow shells on a WEF, under the combined effects of shear deformation, curvature-induced nonlinear coupling, material distribution, layering arrangement, and foundation rigidity is investigated. The developed model has direct application potential in the design of lightweight, rigid, and vibration-resistant spacecraft bodies, satellite antennas and reflectors, launch vehicle shells, aircraft randoms, aerodynamic coatings, and curved fuselage panels, as it allows for the determination of layering arrangements and nanocomposite distributions that can move the resonance region away from critical operating frequencies. The obtained analytical amplitude-frequency relationships physically reveal the interactions between material, geometry, support, and excitation parameters controlling nonlinear resonance, providing a reliable theoretical basis for reduced-order dynamic modeling, resonance tracking, vibration control, and model-based structural condition assessment.

The study consists of five sections. In the second section, the mathematical model of the problem is formulated, defining the fundamental properties of FG-NC layers and the kinematic relationships of doubly curved layered shells within SDT. In the third section, the governing equations of the system are derived within SDT. In the fourth section, the solution process is detailed, and the boundary conditions, approximation functions, and Multiple Time Scales (MTS) method are explained. In the fifth and final section, the numerical results are presented, and the findings are evaluated.

2. Theoretical Developments

This study addresses a doubly curved laminated shell made of FG-NC layers, each composed of a polymer matrix reinforced with CNTs embedded within the matrix, supported by a Winkler elastic basis under an external excitation load $q(x,y,t)$ (Fig. 1a). To define the geometric properties of the structure, a curved orthogonal $Oxyz$ coordinate system located on the mid-surface is used. The shell surface has curvature in two directions, with characteristic dimensions a and b, and radii of curvature R_1 and R_2. The structure, with a total thickness of h, consists of N nanocomposite layers, each with a thickness of $h_0 (= h/N)$ (Fig. 1b). Assuming complete adhesion between the layers forming the laminated structure, it is assumed that the layers move together during deformation, that no discontinuities occur at the interfaces, and that mechanical loads are transmitted continuously throughout the thickness.

2.1. Fundamental assumptions of the nanocomposite layer

The mechanical anisotropy of each layer is attributed to the directional distribution of CNT reinforcements, leading to an orthotropic constitutive behavior of the nanocomposite medium. Under this assumption, the CNT and matrix volume fractions are related by the following expression [14, 27, 29, 30, 31]:

$$V_{cn}^{(k)} + V_{m}^{(k)} = 1 \tag{1}$$

To characterize the stiffness of the nanocomposite medium, the effective elasticity moduli, Poisson ratio and density are calculated by employing the extended rule of mixtures, yielding the following expressions [14, 27, 29, 30, 31]:

$$\begin{aligned}
&E_{11NC}^{(k)} = \eta_1^{(k)} V_{\bar{z}cn}^{(k)} E_{11cn}^{(k)} + V_m^{(k)} E_m^{(k)}, \ \frac{\eta_2^{(k)}}{E_{22NC}^{(k)}} = \frac{V_{\bar{z}cn}^{(k)}}{E_{22cn}^{(k)}} + \frac{V_m^{(k)}}{E_m^{(k)}}, \ \frac{\eta_3^{(k)}}{G_{12NC}^{(k)}} = \frac{V_{\bar{z}cn}^{(k)}}{G_{12cn}^{(k)}} + \frac{V_m^{(k)}}{G_m^{(k)}}, \\
&G_{13NC}^{(k)} = G_{12NC}^{(k)}, \ G_{23NC}^{(k)} = 1.2 G_{12NC}^{(k)}, \ \nu_{12}^{(k)} = V_{cn}^{*(k)} \nu_{12cn}^{(k)} + V_m^{(k)} \nu_m^{(k)}, \ \rho_t^{(k)} = V_{cn}^{*(k)} \rho_{cn}^{(k)} + V_m^{(k)} \rho_m^{(k)} \\
&z = \bar{z}h, \ -\frac{1}{2} + \frac{k-1}{N} \le \bar{z} \le -\frac{1}{2} + \frac{k}{N}, \ k = 1,2,...,N
\end{aligned} \tag{2}$$

where $E_{iiNC}^{(k)}, G_{12NC}^{(k)}, G_{13NC}^{(k)}, G_{23NC}^{(k)} (i = 1,2, \ k = 1,2,3)$ denote the effective Young's and shear moduli of the k^{th} nanocomposite layer. The quantities $E_{iicn}^{(k)}, G_{12cn}^{(k)}, G_{13cn}^{(k)}, G_{23cn}^{(k)} (i = 1,2, \ k = 1,2,3)$ correspond to the elastic properties of the CNT reinforcements, while $E_m^{(k)}$, $G_m^{(k)}$ represent those of the matrix material. Together, these parameters define the equivalent mechanical characteristics of the k^{th} layer in the doubly curved laminated shell. $\nu_{12cn}^{(k)}$ and $\nu_m^{(k)}$ are the Poisson's ratios, $\rho_{cn}^{(k)}$ and $\rho_m^{(k)}$ are the mass densities of the CNT and matrix, respectively. To incorporate nanoscale effects, the CNT efficiency parameters $\eta_j^{(k)} (j = 1,2,3)$ are identified from molecular dynamics-based calibration of the extended Voigt model.

To characterize the reinforcement pattern across the thickness, the CNT volume fraction in the k^{th} nanocomposite layer is assumed to follow a predefined distribution scheme. The corresponding expression can be written as [14, 27, 29, 30, 31]:

$$U: V_{cn}^{(k)} = V_{cn}^{*(k)}, \quad O: \ V_{\bar{z}cn}^{(k)} = 2\left(1 - 2\left|\bar{z}\right|\right) V_{cn}^{*(k)}, \quad X: V_{\bar{z}cn}^{(k)} = 4\left|\bar{z}\right| V_{cn}^{*(k)} \tag{3}$$

where $V_{cn}^{*(k)}$ corresponds to the overall volume fraction of CNTs incorporated into each nanocomposite layer as reinforcement. Its value is obtained using the following relationship:

$$V_{cn}^{*(k)} = \frac{m_{cn}^{(k)}}{m_{cn}^{(k)} + \left[\rho_{cn}^{(k)} / \rho_m^{(k)}\right]\left[1 - m_{cn}^{(k)}\right]} \tag{4}$$

In this expression, $m_{cn}^{(k)}$ denotes the mass fraction of CNTs in each layer. The nanocomposite distributions in the layers are modeled as uniform (U) and based on shape similarity, as (X) and (O) patterns (Fig. 2).

These distributions have a direct influence on the bending and shear stiffness of the shell. X-type distribution provides advantages in bending problems where surface stresses are dominant, whereas the O-type distribution is preferred in thick shells where shear deformation plays a significant role.

2.2. Kinematics and fundamental assumptions of doubly curved layered FG-NC shell surfaces

In establishing the fundamental kinematic relations, the geometrically based assumptions of the shear deformation theory developed for homogeneous anisotropic shells are adopted; these assumptions are employed in their extended form for functionally graded and nanocomposite layered shells [2, 17]. In this context, the shell kinematics are based on the following fundamental assumptions. Under the assumptions of the shear deformation theory proposed by Ambartsumyan [2], the displacement field is defined by the following relations, generalized for FG-NC laminated shells:

$$\varepsilon_{33} = \frac{\partial u_z}{\partial z} = 0,\ u_z(x,y,t) = w(x,y,t) \tag{5}$$

$$\sigma_{i3}^{(k)} = \frac{\mathrm{d}f_i^{(k)}}{\mathrm{d}z}\Psi_i(x,y,t),\ (i=1,2) \tag{6}$$

where ε_{33} is the normal strain in the z-direction, $u_z(x,y,t) = w(x,y,t)$ is the displacement component in the direction normal to the mid-surface, $\sigma_{i3}^{(k)}(i=1,2)$ are the transverse shear stresses, $\Psi_i(x,y,t)$ are functions associated with the rotation angles, while the functions $f_i^{(k)}(z)$ are geometric weighting functions that define the through-thickness distribution of transverse shear stresses. The vanishing of these functions at the surfaces corresponds to the natural satisfaction of free boundary conditions.

Within this framework, the stress–strain relations for the k^{th} FG-NC layer is defined in accordance with the generalized Hooke's law as follows [17]:

$$\begin{bmatrix}\sigma_{11}^{(k)}\\ \sigma_{22}^{(k)}\\ \sigma_{12}^{(k)}\end{bmatrix} = \begin{bmatrix}Y_{11\bar{z}}^{(k)} & Y_{12\bar{z}}^{(k)} & 0\\ Y_{21\bar{z}}^{(k)} & Y_{22\bar{z}}^{(k)} & 0\\ 0 & 0 & Y_{66\bar{z}}^{(k)}\end{bmatrix}\begin{bmatrix}\varepsilon_{11}\\ \varepsilon_{22}\\ \gamma_{12}\end{bmatrix} \tag{7}$$

and

$$\begin{bmatrix}\sigma_{13}^{(k)}\\ \sigma_{23}^{(k)}\end{bmatrix} = \begin{bmatrix}Y_{55\bar{z}}^{(k)} & 0\\ 0 & Y_{44\bar{z}}^{(k)}\end{bmatrix}\begin{bmatrix}\gamma_{13}\\ \gamma_{23}\end{bmatrix} \tag{8}$$

Here, $\sigma_{ij}^{(k)}$ are the stress components in the k^{th} layer, while ε_{ii} and γ_{ij} represent the corresponding strain components. The $Y_{ij}^{(k)}$ are expressed as follows:

$$\begin{aligned} &Y_{11\bar{z}}^{(k)} = \frac{E_{1\bar{z}}^{(k)}}{1-\nu_{12}^{(k)}\ \nu_{21}^{(k)}},\ Y_{22z_0}^{(k)} = \frac{E_{2\bar{z}}^{(k)}}{1-\nu_{12}^{(j)}\ \nu_{21}^{(j)}}, Y_{12\bar{z}}^{(k)} = \nu_{21}^{(k)}Y_{11\bar{z}}^{(k)} = \nu_{12}^{(k)}Y_{22\bar{z}}^{(k)} = Y_{21\bar{z}}^{(k)},\\ &Y_{44\bar{z}}^{(k)} = G_{23\bar{z}}^{(k)},\ Y_{55\bar{z}}^{(k)} = G_{13\bar{z}}^{(k)},\ Y_{66\bar{z}}^{(k)} = G_{12\bar{z}}^{(k)}. \end{aligned} \tag{9}$$

Substituting relations (6) into relation (8), the transverse shear deformations of the doubly curved FG-NC laminated shell surface take the following form:

$$\gamma_{13} = \frac{\mathrm{d}f_1^{(k)}}{\mathrm{d}z}\frac{\Psi_1}{G_{13\bar{z}}^{(k)}},\ \gamma_{23} = \frac{\mathrm{d}f_2^{(k)}}{\mathrm{d}z}\frac{\Psi_2}{G_{23\bar{z}}^{(k)}}. \tag{10}$$

Based on the fundamental assumptions of the SDT, the relations given in (8) are rearranged and expressed in the following form:

$$\frac{\partial u_x}{\partial z} = -\frac{\partial w}{\partial x} + \gamma_{13},\ \frac{\partial u_y}{\partial z} = -\frac{\partial w}{\partial y} + \gamma_{23} \tag{11}$$

The relations given in (11) clearly describe the variation of the displacement fields defined through the thickness of doubly curved laminated FG-NC shell surfaces with respect to the thickness coordinate z. By substituting the expressions in (8) into the relations in (11) and integrating with respect to z over the interval $(0,z)$, the explicit expressions for the displacement components in the x- and y-directions at any point of the doubly curved laminated FG-NC shell surface are obtained as follows:

$$u_x(x,y,t) = u(x,y,t) - z\frac{\partial w(x,y,t)}{\partial x} + I_1^{(k)}\Psi_1,$$
$$u_y(x,y,t) = v(x,y,t) - z\frac{\partial w(x,y,t)}{\partial y} + I_2^{(k)}\Psi_2. \tag{12}$$

where

$$I_1^{(k)} = \int_0^z \frac{\mathrm{d}f_1^{(k)}}{\mathrm{d}z}\frac{\Psi_1}{G_{13\bar{z}}^{(k)}}dz, \quad I_2^{(k)} = \int_0^z \frac{\mathrm{d}f_2^{(k)}}{\mathrm{d}z}\frac{\Psi_2}{G_{23\bar{z}}^{(k)}}dz. \tag{13}$$

The displacement field is formulated by accounting for transverse shear deformation effects through the shell thickness. Using the assumptions $u_x = u(x,y,t)$ and $u_y = v(x,y,t)$ the reference surface, substitution of Eq. (12) into Eq. (11) leads to the strain–displacement relations for the doubly curved laminated FG-NC shell:

$$\varepsilon_{11} = \varepsilon_{11}^0 - z\frac{\partial^2 w}{\partial x^2} + I_1^{(k)}\frac{\partial \Psi_1}{\partial x},\ \varepsilon_{22} = \varepsilon_{22}^0 - z\frac{\partial^2 w}{\partial y^2} + I_2^{(k)}\frac{\partial \Psi_2}{\partial y},$$
$$\gamma_{12} = \gamma_{12}^0 - 2z\frac{\partial^2 w}{\partial x \partial y} + I_1^{(k)}\frac{\partial \Psi_1}{\partial y} + I_2^{(k)}\frac{\partial \Psi_2}{\partial x}. \tag{14}$$

Here ε_{11}^0 and ε_{22}^0 denote the NL deformation components of the reference surface of the laminated cylindrical shell in the x - and y -directions, respectively, while γ_{12}^0 represents the NL shear deformation on the reference surface and the following definitions apply [2-6]:

$$\varepsilon_{11}^0 = \frac{\partial u}{\partial x} - \frac{w}{R_1} + \frac{1}{2}\left(\frac{\partial w}{\partial x}\right)^2,\ \varepsilon_{22}^0 = \frac{\partial v}{\partial y} - \frac{w}{R_2} + \frac{1}{2}\left(\frac{\partial w}{\partial y}\right)^2,\ \gamma_{12}^0 = \frac{\partial u}{\partial y} + \frac{\partial v}{\partial x} + \frac{\partial w}{\partial x}\frac{\partial w}{\partial y}. \tag{15}$$

By substituting the relations for the deformation components given in Eq. (15) into Eq. (8), the stress–strain relations of the shell can be reformulated in terms of the reference surface variables as follows:

$$\begin{bmatrix}\sigma_{11}^{(k)}\\ \sigma_{22}^{(k)}\\ \gamma_{12}^{(k)}\end{bmatrix} = \begin{bmatrix}\bar{Y}_{11\bar{z}}^{(k)} & \bar{Y}_{12\bar{z}}^{(k)} & 0\\ \bar{Y}_{21\bar{z}}^{(k)} & \bar{Y}_{22\bar{z}}^{(k)} & 0\\ 0 & 0 & Y_{66\bar{z}}^{(k)}\end{bmatrix}\begin{bmatrix}\varepsilon_{11}^0 - z\dfrac{\partial^2 w}{\partial x^2}\\ \varepsilon_{22}^0 - z\dfrac{\partial^2 w}{\partial y^2}\\ \gamma_{12}^0 - 2z\dfrac{\partial^2 w}{\partial x \partial y}\end{bmatrix} + \begin{bmatrix}\bar{Y}_{11\bar{z}}^{(k)} & 0 & 0\\ \bar{Y}_{21\bar{z}}^{(k)} & 0 & 0\\ 0 & 0 & \bar{Y}_{15}^{(k)}\end{bmatrix}\begin{bmatrix}\dfrac{\partial \Psi_1}{\partial x}\\ 0\\ \dfrac{\partial \Psi_1}{\partial y}\end{bmatrix} + \begin{bmatrix}\bar{Y}_{12\bar{z}}^{(k)} & 0 & 0\\ \bar{Y}_{22\bar{z}}^{(k)} & 0 & 0\\ 0 & 0 & \bar{Y}_{18\bar{z}}^{(k)}\end{bmatrix}\begin{bmatrix}\dfrac{\partial \Psi_2}{\partial y}\\ 0\\ \dfrac{\partial \Psi_2}{\partial x}\end{bmatrix}. \tag{16}$$

In the expressions obtained from this formulation, it is observed that the terms associated with transverse shear deformation functions explicitly incorporate the elastic material properties of the nanocomposite layers. Thus, the CNT reinforcement, elasticity moduli, and anisotropic mechanical characteristics of each layer are directly reflected in the model through the contribution of transverse shear deformations to the stress distribution. The resulting terms can be expressed as follows:

$$\bar{Y}_{11\bar{z}}^{(k)} = I_{1z}^{(k)}Y_{11\bar{z}}^{(k)},\ \bar{Y}_{12\bar{z}}^{(k)} = I_{2z}^{(k)}Y_{12\bar{z}}^{(k)}, \bar{Y}_{21\bar{z}}^{(k)} = I_{1z}^{(k)}Y_{21\bar{z}}^{(k)}, \bar{Y}_{22\bar{z}}^{(k)} = I_{2z}^{(k)}Y_{22\bar{z}}^{(k)}, \bar{Y}_{15\bar{z}}^{(k)} = I_{1z}^{(k)}Y_{66\bar{z}}^{(k)},\ \bar{Y}_{18\bar{z}}^{(k)} = I_{2z}^{(k)}Y_{66\bar{z}}^{(k)}. \tag{17}$$

The force and moment components of doubly curved laminated nanocomposite shell surfaces, based on definitions commonly used in both classical and modern shell theories are expressed as follows [1-6].

$$\left[N_{ij}, Q_i, M_{ij}\right] = \sum_{k=1}^{N}\int_{z_{k-1}}^{z_k}\left[\sigma_{ij}^{(k)},\ \sigma_{i3}^{(k)},\ z\sigma_{ij}^{(k)}\right]\mathrm{d}z\ \ (i,j=1,2). \tag{18}$$

where

$$z_{k-1} = -0.5h + (k-1)hN^{-1},\ z_k = -0.5h + khN^{-1}. \tag{19}$$

The Airy approach allows the equilibrium equations to be satisfied identically and the problem to be formulated with fewer unknowns. Therefore, it is widely used in shell theories, and the force components are expressed in terms of the Airy stress function as follows [1-6]:

$$(N_{11}, N_{22}, N_{12}) = \left(h\frac{\partial^2 \Phi}{\partial y^2}, h\frac{\partial^2 \Phi}{\partial x^2}, -h\frac{\partial^2 \Phi}{\partial x \partial y} \right). \tag{20}$$

3. Governing Equations

The geometrically NL equations of motion of doubly curved laminated shells are reformulated and presented below for use in subsequent analyses of doubly curved layered FG-NC shell surfaces resting on a WEF and subjected to external excitation load [2-6]:

$$\frac{\partial M_{11}}{\partial x} + \frac{\partial M_{12}}{\partial y} - Q_1 + \rho_1 \frac{\partial^3 w}{\partial x \partial t^2} - \rho_2 \frac{\partial^2 \Psi_1}{\partial t^2} = 0, \tag{21}$$

$$\frac{\partial M_{21}}{\partial x} + \frac{\partial M_{22}}{\partial y} - Q_2 + \rho_1 \frac{\partial^3 w}{\partial y \partial t^2} - \rho_3 \frac{\partial^2 \Psi_2}{\partial t^2} = 0, \tag{22}$$

$$\frac{\partial Q_1}{\partial x} + \frac{\partial Q_2}{\partial y} + N_{11}\frac{\partial^2 w}{\partial x^2} + 2N_{12}\frac{\partial^2 w}{\partial x \partial y} + N_{22}\frac{\partial^2 w}{\partial y^2} - \frac{N_{11}}{R_1} - \frac{N_{22}}{R_2} + K_w w + q(x,y,t) = \bar{\rho}\frac{\partial^2 w}{\partial t^2} + 2\xi\bar{\rho}\frac{\partial w}{\partial t}. \tag{23}$$

In these expressions, K_w is the Winkler elastic foundation stiffness coefficient, describing the resistance of the elastic medium to out-of-plane deformation of the shell. Physically, it relates the foundation reaction force per unit area to the corresponding normal displacement, and its unit is $\mathrm{N/m^3}$, ξ is the viscous damping coefficient, and $\rho_1, \rho_2, \rho_3, \bar{\rho}$ are the symbols used for density, which are defined as follows:

$$\bar{\rho} = \sum_{k=1}^{N} \int_{z_{k-1}}^{z_k} \rho_t^{(k)} \mathrm{d}z,\ \rho_1 = \sum_{k=1}^{N} \int_{z_{k-1}}^{z_k} \rho_t^{(k)} z^2 \mathrm{d}z,\ \rho_2 = \sum_{k=1}^{N} \int_{z_{k-1}}^{z_k} I_{1z}^{(k)} \rho_t^{(k)} z \mathrm{d}z,\ \rho_3 = \sum_{k=1}^{N} \int_{z_{k-1}}^{z_k} I_{2z}^{(k)} \rho_t^{(k)} z \mathrm{d}z. \tag{24}$$

The kinematic compatibility requirement for the doubly curved shell, accounting for von Kármán geometric nonlinearities, is given by [2-6]:

$$\frac{\partial^2 \varepsilon_{11}^0}{\partial y^2} + \frac{\partial^2 \varepsilon_{22}^0}{\partial x^2} - \frac{\partial^2 \gamma_{12}^0}{\partial x \partial y} + \frac{1}{R_2}\frac{\partial^2 w}{\partial x^2} + \frac{1}{R_1}\frac{\partial^2 w}{\partial y^2} - \left(\frac{\partial^2 w}{\partial x \partial y} \right)^2 + \frac{\partial^2 w}{\partial x^2}\frac{\partial^2 w}{\partial y^2} = 0 \tag{25}$$

Following the successive substitution (16) and (18) into the governing relations (21)–(23) and (25), and taking (20) into consideration, the complete set of governing equations is obtained. The resulting formulation describes the coupled dynamic and compatibility behavior of the doubly curved laminated FG-NC shell–foundation system according to SDT:

$$L_{11}\Phi + L_{12}\Psi_1 + L_{13}\Psi_2 + L_{14}w = 0 \tag{26}$$

$$L_{21}\Phi + L_{22}\Psi_1 + L_{23}\Psi_2 + L_{24}w = 0 \tag{27}$$

$$L_{31}\Phi + L_{32}\Psi_1 + L_{33}\Psi_2 + L_{34}w + NL_3(\Phi, w) = q(x,y,t) \tag{28}$$

$$L_{41}\Phi + L_{42}\Psi_1 + L_{43}\Psi_2 + L_{44}w + NL_4(w, w) = 0 \tag{29}$$

where L_{ij}, NL_3, NL_4 are linear and nonlinear operators and are defined in Appendix A.

4. Solution Procedure

4.1 Boundary conditions and admissible approximation functions

Within the formulation developed in this study, since all boundary edges of the doubly curved laminated FG–NC shell are assumed to be simply supported, the boundary conditions are defined as follows [2, 4–6, 17]:

$$\begin{aligned} &w = 0,\ M_{11} = 0,\ \Psi_2 = 0 \ \text{ at } x = 0 \text{ and } a \\ &w = 0,\ M_{22} = 0,\ \Psi_1 = 0 \ \text{ at } y = 0 \text{ and } b \end{aligned} \tag{30}$$

The admissible functions are chosen so that the transverse displacement $w(x,y,t)$ automatically satisfies the boundary conditions at all edges. For the rotational components Ψ_1 and Ψ_2, appropriate sine–cosine combinations are adopted, ensuring both satisfaction of the support constraints and preservation of the modal form of the governing equations after differentiation.

The selected approximation functions are expressed as follows [2, 4-6]:

$$w(x,y,t) = W(t)\sin(\bar{m}x)\sin(\bar{n}y),\ \Psi_1(x,y,t) = \Psi_{10}(t)\cos(\bar{m}x)\sin(\bar{n}y),\ \Psi_2(x,y,t) = \Psi_{20}(t)\ \sin(\bar{m}x)\cos(\bar{n}y). \tag{31}$$

Here, $W(t)$, $\Psi_{10}(t)$ and $\Psi_{20}(t)$ can be interpreted as the generalized coordinates of the dynamic system obtained through the Galerkin reduction procedure, and they represent the fundamental time-dependent unknown functions governing the dynamic stability behavior of the shell. $\bar{m} = m\pi / a$ and $\bar{n} = n\pi / b$ in which m and n represent the corresponding mode numbers in these directions.

It is mathematically demonstrated in Appendix B that the approximation functions defined in Eq. (31) satisfy the boundary conditions given in Eq. (30).

The particular solution of the equation obtained by substituting Eq. (31) into the compatibility equation (29), is obtained in the following fo rm:

$$\Phi = e_1\cos(2\bar{m}x) + e_2\cos(2\bar{n}y) + e_3\sin(\bar{m}x)\sin(\bar{n}y) \tag{32}$$

The coefficients appearing in Eq. (35), obtained for the Airy stress function, represent the geometric, kinematic, and material parameters used in this study, and the manner in which each coefficient is utilized is explicitly defined below:

$$e_1 = \frac{\bar{n}^2 W^2}{32\bar{m}^2 B_{22} h},\ e_2 = \frac{\bar{m}^2 W^2}{32\bar{n}^2 B_{11} h},\ e_3 = \frac{\mu_1 W + \mu_2 \Psi_{10} + \mu_3 \Psi_{20}}{h\left[B_{11}\bar{m}^4 + (B_{12} + B_{21} + B_{31})\bar{m}^2\bar{n}^2 + B_{22}\bar{n}^4\right]} \tag{33}$$

The symbols appearing in these definitions are introduced below in order to clarify the meaning of the quantities used in the equations.

$$\begin{aligned} &\mu_1 = B_{23}\bar{m}^4 + (B_{24} + B_{13} - B_{32})\bar{m}^2\bar{n}^2 + B_{14}\bar{n}^4 + \bar{m}^2 R_2^{-1} + \bar{n}^2 R_1^{-1}, \\ &\mu_2 = -B_{25}\bar{m}^3 - (B_{15} + B_{35})\bar{m}\bar{n}^2,\ \mu_3 = -(B_{28} + B_{38})\bar{m}^2\bar{n} - B_{18}\bar{n}^3. \end{aligned} \tag{34}$$

4.2. Nonlinear motion equation

At this stage, in order to examine the dynamic response of the derived NL governing equations not only under free vibration conditions but also under external excitations, the time-dependent external loading acting on the shell system is introduced. The harmonic transverse excitation load is defined as follows [3, 6]:

$$q(x,y,t) = q_0\sin(m_1 x)\sin(m_2 y)\cos(\Omega t) \tag{35}$$

where Ω and q_0 denote the angular frequency and amplitude of the external excitation, respectively.

The approximation functions given in equations (31) and (33) were fitted into the governing partial differential equations defined in the surface region $\{0 \le x \le a,\ 0 \le y \le b\}$, and the resulting expressions were integrated over the weight functions over the entire problem region using the Galerkin method, taking into account relation (35). Then, by eliminating the variables $\Psi_{10}(t)$ and $\Psi_{20}(t)$ from the equation system, the following ordinary differential equation was obtained, which describes the damped nonlinear dynamic behavior of doubly curved laminated FG-NC shells on a WEF in the SDT frame.

$$\frac{\mathrm{d}^2 W}{\mathrm{d}t^2} + 2\xi \frac{\mathrm{d}W}{\mathrm{d}t} + \left(\omega_w^{st}\right)^2 W + \lambda_1^{NL} W^2 + \lambda_2 W^3 - \lambda_3 q_0 \cos(\Omega t) = 0 \tag{36}$$

Here, $\omega = \omega_w^{st}$ is the linear frequency of doubly curved laminated FG-NC shallow shells on a WEF within SDT, and is expressed by the following relation:

$$\omega_w^{st} = \sqrt{\frac{1}{U_{23}\bar{\rho}}\left[U_{31}^{w}U_{23} - U_{21}U_{34} + \frac{(U_{23}U_{33} - U_{22}U_{34})(U_{11}U_{23} - U_{21}U_{13})}{U_{22}U_{13} - U_{23}U_{12}}\right]} \tag{37}$$

$$\lambda_1^{NL} = \frac{1}{S_{23}\bar{\rho}}\left[U_{31}^{NL}U_{23} - U_{34}U_{21}^{NL} + \frac{(U_{34}U_{22} - U_{23}U_{33})\left(U_{11}^{NL}U_{23} - U_{13}U_{21}^{NL}\right)}{U_{12}U_{23} - U_{13}U_{22}}\right], \lambda_2 = \frac{U_{32}}{\bar{\rho}},\ \lambda_3 = \frac{1}{\bar{\rho}} \tag{38}$$

where the coefficients U_{ij} involved in (37) and (38) are given in Appendix C.

4.3. Solution formulation based on the multiple time scales method

Eq. (36) is analyzed under primary resonance conditions using the method of multiple time scales. In this approach, damping, external excitation, and nonlinear effects are treated as small perturbations, allowing the response to be represented as an asymptotic expansion in terms of the perturbation parameter ε. This formulation enables the systematic separation of terms at different orders and the elimination of secular contributions, thereby yielding a uniformly valid solution over extended time intervals. The analysis is performed assuming that the system starts from its maximum displacement position with zero initial velocity, leading to the following initial conditions [2-6, 25, 26]:

$$W = w_{\max}, \frac{\mathrm{d}W}{\mathrm{d}t} = 0 \ \text{ when } t = 0\,. \tag{39}$$

The adopted initial conditions define a stationary configuration at $t = 0$, from which the evolution of the shell's nonlinear forced vibration behavior is determined.

To apply the multiple time scale method to Eq. (36), it is assumed that the damping and external excitation effects present in the system are small compared to the vibration amplitude. For this purpose, a small perturbation parameter ε is defined, and the damping and harmonic forcing load terms are evaluated at the order of $O(\varepsilon^2)$, while the nonlinear contributions were separated into different orders depending on the magnitude of their effects. Accordingly, quadratic nonlinearity is considered at the level of $O(\varepsilon)$, and cubic nonlinearity at the level of $O(\varepsilon^2)$ $O(\varepsilon^2)$. As a result of this scaling, the expressions $2\xi \frac{\mathrm{d}W}{\mathrm{d}t} = 2\varepsilon^2 \bar{\xi} \frac{\mathrm{d}W}{\mathrm{d}t}$ and $\lambda_3 q_0 \cos(\Omega t) = \varepsilon^2 q_3 \cos(\Omega t)$ are obtained, while the nonlinear terms are redefined as $q_1 W^2 = \varepsilon q_1 W^2$ and $q_2 W^3 = \varepsilon q_2 W^3$. In addition, in order to investigate the primary resonance region, it was assumed that the external forcing frequency is quite close to the linear natural frequency of the system. As a result of those adjustments, (36) is transformed into a form suitable for perturbation analysis and made ready for the application of the multiple time scales method.

$$\frac{\mathrm{d}^2W}{\mathrm{d}t^2}+\left(\omega_w^{st}\right)^2 W=-2\varepsilon^2\bar{\xi}\frac{\mathrm{d}W}{\mathrm{d}t}-\varepsilon q_1W^2-\varepsilon^2 q_2W^3+\varepsilon^2 q_3\cos\left(\Omega t\right) \tag{40}$$

where

$$\bar{\xi}=\frac{\xi}{\varepsilon^2},\ q_1=\frac{\lambda_1^{NL}}{\varepsilon},\ q_2=\frac{\lambda_2}{\varepsilon^2},q_3=\frac{\lambda_3 q_0}{\varepsilon^2} \tag{41}$$

Under primary resonance conditions, the excitation frequency Ω is assumed to differ only slightly from the linear natural frequency. Introducing the detuning parameter σ, this relationship can be expressed as [25]:

$$\Omega=\omega_w^{st}+\varepsilon^2\sigma \tag{42}$$

Such a representation enables the resonant interaction between the excitation and the fundamental mode to be captured while preserving the asymptotic ordering of the perturbation scheme. Consequently, the combined influences of damping, nonlinearities, and external excitation can be systematically evaluated over extended time intervals within the multiple time scales framework [25, 26]. To proceed with the perturbation analysis, the solution of Eq. (40) is sought in the form of an asymptotic expansion with respect to the small parameter ε:

$$W(T,\varepsilon)=W_0(T_0,T_1,T_2)+\varepsilon W_1(T_0,T_1,T_2)+\varepsilon^2W_2(T_0,T_1,T_2)+... \tag{43}$$

Within the multiple time scales framework, the independent variables $T_0=t$, $T_1=\varepsilon t$ and $T_2=\varepsilon^2 t$ are introduced to capture the response components evolving over distinct temporal scales. Here, T_0 corresponds to the rapid oscillatory motion governed primarily by the system's linear natural frequency.

The application of the perturbation procedure transforms Eq. (40) into a series of coupled equations organized according to the magnitude of ε. Enforcing the equality of terms at each order yields the governing relations at $O(1)$, $O(\varepsilon)$ and $O(\varepsilon^2)$, respectively.

$$O(1):D_0^2W_0+\left(\omega_w^{st}\right)^2W_0=0 \tag{44}$$

$$O(\varepsilon):D_0^2W_1+\left(\omega_w^{st}\right)^2W_1=-2D_0D_1W_0-q_1W_0^2 \tag{45}$$

$$\begin{aligned}&O(\varepsilon^2):D_0^2W_2+\left(\omega_w^{st}\right)^2W_2=-2D_0D_1W_1-(2D_0D_2+D_1^2+2\bar{\xi}D_0)W_0\\&-2q_1W_0W_1-q_2W_0^3+q_3\cos(\omega_w^{st}T_0+\sigma T_2)\end{aligned} \tag{46}$$

The roots of characteristic equation associated with Eq. (44) are obtained as $r=\pm i\omega_w^{st}$. Accordingly, the general solution of the equation at order $O(1)$ can be expressed in complex exponential form as follows:

$$W_0=A(T_1,T_2)e^{i\omega_w^{st}T_0}+\bar{A}(T_1,T_2)e^{-i\omega_w^{st}T_0} \tag{47}$$

Here, $A(T_1,T_2)$ denotes the complex amplitude function, while $\bar{A}(T_1,T_2)$ represents its complex conjugate. This formulation is used to ensure that the solution is real-valued. Since the physical displacement W_0 must be a real quantity, including the complex conjugate term guarantees that the solution remains real.

Let us substitute the expression given in Eq. (47) into Eq. (45):

$$\begin{aligned}&D_0^2W_1+\left(\omega_w^{st}\right)^2W_1=-2i\omega_w^{st}\frac{\partial A(T_1,T_2)}{\partial T_1}e^{iT_0\omega_w^{st}}+2i\omega_w^{st}\frac{\partial A(T_1,T_2)}{\partial T_1}e^{-iT_0\omega_w^{st}}\\&-q_1A^2(T_1,T_2)e^{2iT_0\omega_w^{st}}-q_1A^2(T_1,T_2)e^{-2iT_0\omega_w^{st}}-2q_1\left|A\right|^2\end{aligned} \tag{48}$$

In Eq. (48), the secular terms—namely those proportional to $e^{\pm i\omega_w^{st}T_0}$ vanish completely, and it reduces to:

$$D_0^2 W_1 + \left(\omega_w^{st}\right)^2 W_1 = -2q_1 |A|^2 - q_1 |A|^2 e^{2iT_0\omega_w^{st}} - q_1 \left|\bar{A}\right|^2 e^{-2iT_0\omega_w^{st}} \tag{49}$$

The final form of the particular solution for W_1 is obtained as:

$$W_1 = \frac{q_1}{3\left(\omega_w^{st}\right)^2}\left(-6A(T_2)\bar{A}(T_2) + A^2(T_2)e^{2iT_0\omega_w^{st}} + \bar{A}^2(T_2)e^{-2iT_0\omega_w^{st}}\right) \tag{50}$$

We now consider the equation at order $O(\varepsilon^2)$, i.e., Eq. (46). Using the adopted scaling, that can be rewritten at order $O(\varepsilon^2)$ as follows:

$$\begin{aligned} D_0^2 W_2 + \left(\omega_w^{st}\right)^2 W_2 = & \left[-2i\omega_w^{st} A_{,T_2} - 2\bar{\xi} i\omega_w^{st} A - 3q_2 |A|^2 A + \frac{10}{3}\frac{q_1^2}{\left(\omega_w^{st}\right)^2}|A|^2 A + \frac{q_3}{2}e^{i\sigma T_2} \right] e^{i\omega_w^{st} T_0} \\ & + \left[2i\omega_w^{st} A_{,T_2} + 2\bar{\xi} i\omega_w^{st} A - 3\theta_2 |A|^2 A + \frac{10}{3}\frac{q_1^2}{\left(\omega_w^{st}\right)^2}|A|^2 A + \frac{q_3}{2}e^{-i\sigma T_2} \right] e^{-i\omega_w^{st} T_0} \\ & + (\text{Non - resonant constants and } 2\omega_w^{st} \text{harmonics}) + (3\omega_w^{st} \text{harmonics} = \text{NST}) \end{aligned} \tag{51}$$

Here, the abbreviated notation NST (non-secular terms) refers to the $3\omega_w^{st}$ harmonic components, namely the terms $-q_2 A^3 e^{3iT_0\omega_w^{st}} - q_2 \bar{A}^3 e^{-3iT_0\omega_w^{st}}$ together with the $3\omega_w^{st}$ contributions arising from $W_0 W_1$. These terms originate from Eq. (51). In order to prevent unbounded growth of the solution, the coefficient of $e^{iT_0\omega_w^{st}}$ in Eq. (51) must vanish:

$$-2i\omega_w^{st} A_{,T_2} - 2\bar{\xi} i\omega_w^{st} A - 3q_2 |A|^2 A + \frac{10}{3}\frac{q_1^2}{\left(\omega_w^{st}\right)^2}|A|^2 A + \frac{q_3}{2}e^{i\sigma T_2} = 0 \tag{52}$$

This condition represents the $O(\varepsilon^2)$ solvability condition corresponding to Eq. (52), i.e., the complex amplitude equation, and it automatically includes its complex conjugate counterpart as well. Eq. (52) represents the complex amplitude equation (solvability condition) governing the system behavior in the primary resonance region, and it describes how the amplitude and phase evolve over the slow time scale T_2. However, since $A(T_2)$ is a complex quantity, Eq. (52) is not directly interpretable in a physical sense. In particular, to extract physically meaningful quantities such as steady-state amplitude, phase lag, and the detuning–amplitude relationship in a forced vibration problem, Eq. (52) must be separated into its real and imaginary parts. For this purpose, the complex amplitude $A(T_1, T_2)$ is expressed in amplitude–phase (polar) form as:

$$A(T_1, T_2) = \frac{1}{2}a(T_1)e^{i\theta(T_2)} \tag{53}$$

and

$$\bar{A}(T_1, T_2) = \frac{1}{2}a(T_1)e^{-i\theta(T_2)} \tag{54}$$

The magnitude of the amplitude is then given by

$$|A|^2 = A \cdot \bar{A} = \frac{1}{4}a^2 \tag{55}$$

Using these definitions, the leading-order response W_0, defined at order $O(1)$ by $W_0(T_1, T_2) = A(T_1, T_2)e^{i\omega_w^{st} T_0} + \bar{A}(T_1, T_2)e^{-i\omega_w^{st} T_0}$ can be expressed in fully real form as

$$W_0 = a(T_2)\cos\left[\omega_w^{st} T_0 + \theta(T_2)\right] \tag{56}$$

where $a(T_2)$ represents the vibration amplitude, while $\theta(T_2)$ denotes the phase variation relative to the excitation over the slow time scale.

We now substitute Eq. (53) into Eq. (52) and pass to the polar-coordinate representation, that is, we derive the amplitude–phase equations. For this purpose, we first differentiate $A(T_1, T_2)$ with respect to T_2 :

$$A_{,T_2} = \frac{1}{2}\left(a' + ia\theta'\right)e^{i\theta} \tag{57}$$

where $a' = \dfrac{da}{dT_2}$ and $\theta' = \dfrac{d\theta}{dT_2}$. In addition, Eq. (55) can be written as

$$|A|^2 A = \frac{a^3}{8}e^{i\theta} \tag{58}$$

Let us substitute each term separately into Eq. (52).

$$-i\omega_w^{st}\frac{da}{dT_2} + \omega_w^{st} a\frac{d\theta}{dT_2} - i\omega_w^{st} a\bar{\xi} + \frac{a^3}{2}k + \frac{q_3}{2}e^{i(\sigma T_2 - \theta)} = 0 \tag{59}$$

where

$$k = -\frac{3q_2}{4} + \frac{5}{3}\frac{q_1^2}{8(\omega_w^{st})^2} \tag{60}$$

If the phase difference is defined as

$$\gamma = \sigma T_2 - \theta \tag{61}$$

then the last term in Eq. (59), $e^{i(\sigma T_2 - \theta)}$, takes the form $e^{i(\sigma T_2 - \theta)} = e^{i\gamma} = \cos\gamma + i\sin\gamma$.

Let us now separate the real and imaginary parts of Eq. (59). The real part is $\omega_w^{st} a\dfrac{d\theta}{dT_2} + \dfrac{a^3}{2}k + \dfrac{q_3}{2}\cos\gamma = 0$ from which the following expression for $\theta' = \dfrac{d\theta}{dT_2}$ is obtained:

$$\frac{d\theta}{dT_2} = -\frac{a^2}{2\omega_w^{st}}k - \frac{q_3}{2\omega_w^{st} a}\cos\gamma \tag{62}$$

The imaginary part of Eq. (59) is $-i\omega_w^{st}\dfrac{da}{dT_2} - i\omega_w^{st} a\bar{\xi} + \dfrac{q_3}{2}i\sin\gamma = 0$ from which we obtain

$$\frac{da}{dT_2} = -a\bar{\xi} + \frac{q_3}{2\omega_w^{st}}\sin\gamma \tag{63}$$

Furthermore, taking the derivative of the phase difference $\gamma = \sigma T_2 - \theta$ with respect to T_2, and using Eq. (62), we obtain

$$\frac{d\gamma}{dT_2} = \sigma - \frac{d\theta}{dT_2} = \sigma - \frac{a^2}{2\omega_w^{st}}k - \frac{q_3}{2\omega_w^{st} a}\cos\gamma \tag{64}$$

Considering the steady-state condition, where both the amplitude and phase difference are constant, we have

$$\frac{da}{dT_2}=0 \text{ and } \frac{d\gamma}{dT_2}=0 \tag{65}$$

To derive the NL frequency–amplitude relationship, the detuning parameter σmust be determined. For this purpose, the identity $\sin^2\gamma+\cos^2\gamma=1$ is used. Substituting Eqs. (63) and (67), squaring, and summing yields,

$$\left(\frac{2\omega_w^{st}}{q_3}a\bar{\xi}\right)^2+\left[\frac{2\omega_w^{st}a}{q_3}\left(\sigma-\frac{a^2}{2\omega_w^{st}}k\right)\right]^2=1 \tag{66}$$

After simplification, Eq. (66) takes the final form

$$\left(2\omega_w^{st}a\bar{\xi}\right)^2+\left(2\omega_w^{st}\sigma a-ka^3\right)^2=q_3^2 \tag{67}$$

Eq. (67) represents the closed-form response curve for forced primary resonance. From (67), the detuning parameter σ is obtained as follows:

$$\sigma_i=\frac{ka^3\pm\sqrt{q_3^2-\left(2\omega_w^{st}a\bar{\xi}\right)^2}}{2\omega_w^{st}a} \tag{68}$$

where k is the NL coefficient, characterizing hardening ($k>0$) or softening ($k<0$) behavior and q_3 is the forcing amplitude.

Substituting Eq. (68) into Eq. (42), the NL forced frequency–amplitude relationship for doubly curved laminated FG-NC shell surfaces resting on a WEF is obtained as

$$\Omega_{FF_i}^{NLstw}=\omega_w^{st}+\varepsilon^2\frac{ka^3\pm\sqrt{q_3^2-\left(2\omega_w^{st}a\bar{\xi}\right)^2}}{2\omega_w^{st}a},\ (i=1,2) \tag{69}$$

For umerical computations, by introducing the definition $A_{q_1}=a/h$ into the final expression, the equation can be reformulated in the following compact form.:

$$\Omega_{FF_i}^{NLstw}=\omega_w^{st}+\frac{\varepsilon^2}{2\omega_w^{st}hA_{q_1}}\left[k\left(hA_{q_1}\right)^3\pm\sqrt{q_3^2-\left(2\omega_w^{st}hA_{q_1}\bar{\xi}\right)^2}\right] \tag{70}$$

The dimensionless NL forced vibration frequencies of doubly curved FG-NC laminated shells resting on a WEF within SDT can be expressed as follows:

$$\bar{\Omega}_{FF_i}^{NLstw}=\Omega_{FF_i}^{NLstw}h\sqrt{\rho_m^{(1)}/E_m^{(1)}}\ (i=1,2) \tag{71}$$

The ratio of the NL frequency to linear frequency (or NLF/LF) of doubly curved layered FG-NC shells resting on a WEF is defined as follows:

$$\frac{\Omega_{FF_i}^{NLstw}}{\omega_0^{st}}=\frac{\omega_w^{st}}{\omega_0^{st}}+\frac{\varepsilon^2\sigma_i}{\omega_0^{st}},\quad (i=1,2) \tag{72}$$

Below, two important special cases of this general expression are examined separately.

a) Linear limit: For $k=0$ in Eq. (67), which represents the final frequency–amplitude relation of NL forced vibration for doubly curved laminated nanocomposite shell surfaces resting on an elastic foundation, the classical

Lorentz-type response is obtained. It should be emphasized that $k = 0$ corresponds to the case where NL effects are negligible or very small. In this case, Eq. (67) reduces to:

$$\left(2\omega_w^{st} hA_{q_1}\bar{\xi}\right)^2 + \left(2\omega_w^{st}\sigma hA_{q_1}\right)^2 = q_3^2 \tag{73}$$

Factoring out the common term $\left(2\omega_w^{st} hA_{q_1}\bar{\xi}\right)^2$, we obtain: $\left(2\omega_w^{st} hA_{q_1}\right)^2\left(\bar{\xi}^2 + \sigma^2\right) = q_3^2$. From this, the steady-state amplitude is obtained as:

$$A_{q_1}(\sigma) = \frac{q_3}{2h\omega_w^{st}\sqrt{\left(\bar{\xi}^2 + \sigma^2\right)}} \tag{74}$$

Eq. (74) shows that the resonance response is symmetric with respect to the detuning parameter σ. For $\sigma = 0$ (exact resonance), the maximum amplitude is:

$$A_{p_1}^{\max} = \frac{q_3}{2h\omega_w^{st}\bar{\xi}} \tag{75}$$

As $|\sigma|$ increases, the amplitude decreases rapidly, resulting in a bell-shaped curve. Therefore, Eq. (74) is completely identical to the Lorentz-type resonance curve obtained in a classical forced damped linear oscillator.

This expression is known as the Lorentzian response in the frequency domain, and the fact that the resonance response is linear, single-valued, and symmetric is a distinguishing characteristic of linear systems.

b) Backbone curve: The BB curve arises when the excitation is small and represents the frequency shift in the unforced (and ideally undamped) natural vibration of NL system. In other words, when the effect of the external force is not dominant, the frequency shift mainly originates from the intrinsic NL dynamics of the system. Therefore, in deriving the BB curve, the effect of forcing is typically neglected (i.e., $q_3 = 0$), and for the interpretation of free vibration, the damping term is also neglected (i.e., $\bar{\xi} = 0$). Under these assumptions, Eq. (67) transforms into the following form for the detuning parameter:

$$\left(2\omega_w^{st}\sigma hA_{p_1} - kh^3 A_{p_1}^3\right)^2 = 0 \tag{76}$$

Since the dimensionless amplitude $A_{q_1} \neq 0$, dividing both sides by A_{q_1} and solving for the detuning parameter σ yields the following expression for the BB curve:

$$\sigma = \frac{kh^2 A_{q_1}^2}{2\omega_w^{st}} \tag{77}$$

where σ represents the small difference between the excitation frequency and the linear natural frequency:

$$\Omega_{BBw}^{NLst} = \omega_w^{st} + \varepsilon^2\sigma \tag{78}$$

Substituting (77) into (78) shows that the frequency depending on the amplitude due to nonlinearity:

$$\Omega_{BBw}^{NLst} = \omega_w^{st} + \varepsilon^2\frac{k\left(hA_{q_1}\right)^2}{2\omega_w^{st}} \tag{79}$$

Eq. (79) represents the frequency–amplitude relationship for NL free vibration (or BB) of doubly curved laminated nanocomposite shell surfaces resting on an elastic foundation. If $k > 0$, the system exhibits hardening behavior (since $\sigma > 0$ as aincreases), whereas if $k < 0$, it exhibits softening behavior (since $\sigma < 0$ as aincreases).

The BB curve determines the "skeleton" of the forced response curve and clearly indicates the direction in which the resonance peak shifts with increasing amplitude. The dimensionless frequency or BB curve of doubly curved FG-NC layered shells resting on a WEF is defined as follows:

$$\bar{\Omega}_{BBw}^{NLst} = \Omega_{BBw}^{NLst} h\sqrt{\rho_m^{(1)} / E_m^{(1)}} \ (i = 1,2) \tag{80}$$

The ratio of the NLF/L of doubly curved laminated FG-NC shells resting on a WEF is defined as follows:

$$\frac{\Omega_{BBw}^{NLst}}{\omega_0^{st}} = \frac{\omega_w^{st}}{\omega_0^{st}} + \frac{\varepsilon^2 \sigma}{\omega_0^{st}} \tag{81}$$

Special Cases and Limitations of the Model: The NL dynamic model developed in this study provides a general framework for analyzing the vibration behavior of doubly curved FG-NC shell surfaces resting on a WEF. The model can be reduced to several classical cases widely used in the literature by assigning specific values to the elastic foundation parameters and geometric curvatures. This reducibility demonstrates both the generality and the accuracy of the proposed formulation.

When $K_w = 0$, the foundation effect completely vanishes, the resulting equations represent the NL forced vibration characteristics of doubly curved laminated FG-NC shell surfaces without any foundation.

From a geometrical point of view, the case $R_1 = R_2 = R$ corresponds to spherical shell surfaces, while $R_1 = -R_2 = R$ corresponds to hyperbolic paraboloid shell surfaces. Under these special geometric conditions, it is observed that Eqs. (37), (70)-(72) and (79)-(81) obtained for doubly curved laminated FG-NC shells on a WEF, are also valid for spherical and hyperbolic paraboloid shells, respectively. This result indicates that the developed model can encompass different shell geometries within a unified theoretical framework.

5. Numerical Results and Comments

In this section, the accuracy and applicability of the developed NL dynamic model are comprehensively evaluated. Furthermore, the dependence of the NL forced vibration frequency of doubly curved laminated FG-NC shell structures on various system parameters is investigated in detail. As representative geometries of doubly curved laminated shell surfaces, a laminated spherical shell (Fig.3a) and a laminated hyperbolic paraboloid shell (Fig. 3b) on the WEF are considered.

This section is presented under three subheadings. First, the mechanical properties of FG-NC materials used in comparative and numerical analyses are introduced; then, the accuracy of the developed model is evaluated by comparing it with existing results in the literature and Finite Element Method (FEM) solutions. Finally, the nonlinear forced vibration behavior of doubly curved layered FG-NC shells on a WEF is investigated, and the effects of nonlinearity, soil parameters, curvature characteristics, and layer distribution on frequency-amplitude relationships are examined in detail.

5.1. FG-NC material model

In this subsection, the fundamental material properties of FG-NC are modeled. Polymethyl methacrylate (PMMA) is selected as the matrix material. The elastic and physical properties of PMMA are taken as Young's modulus $E_m^{(k)} = 2.5\,\text{GPa}$, Poisson's ratio $\nu_m^{(k)} = 0.34$ and density $\rho_m^{(k)} = 1150\ \text{kg/m}^3$ [13]. As the reinforcement phase, single-walled carbon nanotubes (SWCNTs) of the (10,10) armchair type are employed. The geometric properties of the CNTs are defined as $L_{cn} = 7.26\,\text{nm}, \text{R}_{cn} = 0.68\,\text{nm}, h_{cn} = 0.067\,\text{nm}$. These quantities are assumed to remain constant throughout the entire composite volume. All material parameters are evaluated under a constant temperature condition of $T = 300\,\text{K}$ (room temperature). The typical effective material parameters of CNTs used in this study are calculated according to the values reported in [13, 30]: $E_{11cn}^{(k)} = 5.6466\,\text{TPa}, E_{22cn}^{(k)} = 7.0800\,\text{TPa}, G_{12cn}^{(k)} = 1.9445\,\text{TPa}, \nu_{12cn}^{(k)} = 0.175,\ \rho_{cn}^{(k)} = 1400\,\text{kg/m}^3$. The efficiency parameters are defined as functions of the CNT volume fraction and are employed in the PMMA/CNT reinforcement system: $\eta_1^{(k)} = 0.137,\ \eta_2^{(k)} = 1.022,\ \eta_3^{(k)} = 0.715$ for $V_{cn}^{*(k)} = 0.12$; $\eta_1^{(k)} = 0.142,\ \eta_2^{(k)} = 1.626,\ \eta_3^{(k)} = 1.138$ for $V_{cn}^{*(k)} = 0.17$; $\eta_1^{(k)} = 0.141,\ \eta_2^{(k)} = 1.585,\ \eta_3^{(k)} = 1.109$ for $V_{cn}^{*(k)} = 0.28$. The fundamental material parameters defined above are used as constant inputs in the mathematical model established in the subsequent subsections, and all analyses are carried out based on these parameters. The shear stress distribution through the thickness is represented by the following shape functions: $f^{(k)}_{,z} = 1 - 4\bar{z}^2$ [2, 4].

5.2. Benchmark and comparison examples

In comparison example 1, numerical results obtained from a three-way comparison with two different literature sources, namely Reddy [4] and Nayfeh & Mook [25], are presented in Table 1. The aim of this comparison is to clearly demonstrate that the proposed model is fully consistent, in both trend and order of magnitude, with the classical NL forced vibration literature. In comparison, a special case of Eq. (70), previously derived for doubly curved laminated FG-CNTRC shell surfaces resting on a WEF, is employed. Considering that $K_w = 0$, it follows that $\omega_{wp}^{st} = \omega_0^{st}$ and thus Eq. (70) reduces to the following form:

$$\frac{\Omega_{FF_i}^{NLst}}{\omega_0^{st}} = 1 + \frac{\varepsilon^2}{2\left(\omega_0^{st}\right)^2 hA_{q_1}}\left[kh^3 A_{q1}^3 \pm \sqrt{q_3^2 - \left(2\omega_0^{st} hA_{q_1}\bar{\xi}\right)^2}\right] \tag{82}$$

In Refs. [4] and [25], the following expressions for weakly NL Duffing-type vibrations are obtained, respectively:

$$\frac{\Omega_{FF}^{NLst}}{\omega_0^{st}} = 1 + \hat{C}_2 A_{q_1}^3 \quad \text{and} \quad \frac{\Omega_{FF}^{NLst}}{\omega_0^{st}} \approx 1 + \hat{C}_1 A_{q_1}^2 \ \left(\text{weak nonlinearity}\right) \tag{83}$$

where $\hat{C}_i$ are evaluated based on the normalized coefficients reported in the respective studies.

Using Eqs. (82) and (83), representative parameters are selected to enable a meaningful comparison. Specifically, for weakly NL forced vibrations, the following typical values are considered: the linear natural frequency $\omega_0^{st} = 10$, the small perturbation parameter $\varepsilon = 0.1$, the cubic NL stiffness (hardening) coefficient $k = 5$, the damping coefficient $\xi = 0.02$, the forcing parameter $q_3^2 = 6$, and the vibration amplitudes $A_{q_1} = 0.5, 1.0, 1.5 \text{ and } 2.0$. In the present study, the ratios of NL to linear frequencies and the corresponding percentage differences for all amplitude values are presented in Table 1, in comparison with the results of Refs. [4] and [25]. The differences among the numerical results given in Table 1 are negligible, with the maximum deviation being less than 0.03%. These minor discrepancies arise from differences in shell/plate assumptions and normalized coefficients used in the respective studies and are within an acceptable range.

In comparison example 2, NLF/LF ratios obtained from the proposed mathematical model are compared with the finite element method (FEM) results reported by Singha and Daripa [40], in which shear deformation effects are considered. The comparison is carried out for square, single-layer homogeneous isotropic plates and homogeneous orthotropic cross-ply laminated plates with a stacking sequence of (0°/90°/0°/90°/0°), considering free (unconstrained) boundary conditions. For the structures examined, the geometric ratio is taken as $a/h = 100$. The calculations are performed under the conditions $k = 5$ and $R_1 \to \infty, R_2 \to \infty, K_w = 0$, which correspond to a simplified special case of Eq. (70). The material constants are selected to be fully consistent with those used by Singha and Daripa [40] in order to ensure the validity of the comparison, and the relevant parameters are defined as follows: $E_{11}^{(k)} / E_{22}^{(k)} = 40$, $G_{12}^{(k)} / E_{22}^{(k)} = G_{13}^{(k)} / E_{22}^{(k)} = 0.6$, $G_{23}^{(k)} / E_{22}^{(k)} = 0.5$, $\nu_{12}^{(k)} = 0.25$, $\rho_t^{(k)} = 1$. The NLF/LF ratios obtained from the numerical calculations are presented in Table 2. As observed in Table 2, in the absence of an elastic foundation, the NLF/LF ratios calculated in the present study for both single-layer and multilayer plates show excellent agreement with the FEM results reported in ref. [40]. This agreement confirms, from both mathematical and numerical perspectives, the accuracy of the proposed model and the validity of the developed solution approach.

5.3. Specific analysis

The nonlinear forced vibration characteristics of laminated FG_NC spherical and hyperbolic paraboloid shell surfaces resting on a WEF are investigated using (70) – (72) and (79) – (81). All numerical computations are performed in Maple 13. For brevity, the abbreviations LS-S (laminated spherical surface) and LHP-S (laminated hyperbolic paraboloid surface) are adopted throughout the study. The geometric parameters, layer arrangements, distribution patterns, and stacking sequences considered in the numerical examples are specified in the corresponding figures, tables, and discussion sections. A constant damping ratio of $\bar{\xi} = 0.005$ assumed in all analyses, while the harmonic excitation is defined as $q_0 = A_{q_0} h^2 \rho_m \left(\omega_0^{Lst}\right)^2$ with the amplitude parameter fixed at $A_{q_0} = 0.004$ [41]. To illustrate the influence of the governing parameters on the nonlinear forced vibration response, numerical results are obtained for spherical ($R_1 = R_2$) and hyperbolic paraboloid ($R_1 = -R_2$) surfaces.

The analyses are conducted using the following data: $a/b=0.5$, $a/h=10$, $(m,n)=(1,1)$, $R_2/a=2,$, $V_{cn}^{*(k)}=0.12, K_w=10^9(\mathrm{N/m^3})$ and $\overline{\xi}=0.005$.

In the analyses, three different stacking sequences representing the U-, O-, and X-material distribution patterns, namely (0°/90°/0°) and (90°/0°/90°) are considered to investigate the nonlinear dynamic behavior of both shallow spherical and hypar shells. In the analysis, the following relative variation definitions are employed:

$$\%\Delta_{st}=100\frac{\Omega_{CST}-\Omega_{SDT}}{\Omega_{CST}},\ \%\Delta_{des}=100\frac{\Omega_{FG}-\Omega_{U}}{\Omega_{U}},\ \%\Delta_{lay}=100\frac{\Omega_{Lay}-\Omega_{(0^o)}}{\Omega_{(0^o)}},\%\Delta_{WF}=100\frac{\Omega_{F}-\Omega_{NF}}{\Omega_{NF}}$$

Here, F and NF denote the cases with and without foundation, respectively.

5.3.1. Comparative analysis of SDT-CST for the nonlinear forced vibrations of laminated nanocomposite shallow spherical shells on a WEF

In the following, a comparative analysis is presented for the spherical shell with and without WEF, where the $\Omega_{FF_1}^{NLstw}$, $\Omega_{FF_2}^{NLstw}$ and Ω_{BBw}^{NLst} frequencies are evaluated as the amplitude A_{q_1} increases from 0.05 to 0.5. The analysis is conducted separately for each stacking sequence, with particular emphasis on the effect of the WEF. The evaluations are based on the data presented in Figs. 5-10.

When the nonlinear forced vibration behavior of spherical shells on a WEF is investigated, it is observed that the layer arrangement plays a decisive role in both absolute frequency levels and shear deformation, model type, and sensitivity to ground effects. In general, nonlinear frequency parameters increase as vibration amplitude increases in all arrangements. However, frequency levels and parameter sensitivities show significant differences depending on the layer orientation. The (0°) reference arrangement stands out as the structure with the highest values in terms of absolute frequency level. Therefore, the performance of other arrangements is mostly evaluated relative to the (0°) shell. In particular, outer layers in the 0° direction increase shell rigidity, resulting in higher nonlinear frequencies (Figs. 7 and 8). In contrast, the (90°/0°/90°) arrangement where the outer layers are oriented at 90° gives the lowest frequency levels across the entire amplitude range (Figs. 9 and 10). Frequency reductions of approximately 29–32% for the U-model, 18–22% for the O-model, and in some cases reaching 56% for the X-model are observed. This result demonstrates that the orientation of the outer layers is highly influential on crustal dynamics. When (0°/90°/0°) and (90°/0°/90°) arrangements are considered together, it is seen that the (0°/90°/0°) arrangement, where the outer layers are oriented at 0°, offers higher frequency levels (Figs. 6 and 7). Furthermore, this arrangement is quite sensitive to shear deformation. The difference between the SDT and CST results reaches 35–50%, especially in U and X models, indicating that neglecting shear deformation can lead to significant errors. In contrast, in the (90°/0°/90°) arrangement, the SDT-CST differences generally remain in the 2–6% range, and the effect of shear deformation is quite limited. This suggests that structures with 90° outer layers behave more in line with classical theories.

In terms of the effect of the layer distribution model, both arrangements show that the O-model reduces frequencies while the X-model increases them. However, the magnitude of this effect is much more pronounced in the (0°/90°/0°) arrangement. Especially at low amplitudes, the X-model provides frequency increases reaching approximately 15%, while the O-model causes frequency decreases in the range of approximately 6–13%. In contrast, in the (90°/0°/90°) arrangement, the effects of the O and X models are more limited, generally remaining at the level of a few percentage points. This indicates that structures with outer layers oriented at 0° are more sensitive to material distribution changes (Figs. 5-10).

In terms of the Winkler elastic ground effect, a reverse trend emerges. While the ground support increases frequencies by approximately 1–3% in the (0°/90°/0°) arrangement, this increase reaches 4–7% in the (90°/0°/90°) arrangement. Therefore, the arrangement with a low absolute frequency level (90°/0°/90°) provides relatively more benefit from ground support. In other words, the Winkler soil acts as a mechanism that partially compensates for the low rigidity of structures with a 90° outer layer (Figs. 5-10).

5.3.2. Comparative analysis of SDT and CST for NLF/LF ratio of laminated nanocomposite shallow spherical shells on a WEF

Figs. 11-13 show the behavior of FF_1, FF_2 and BB curve associated with the ratio $\Omega_{FF_1}^{NLstw}/\omega_0^{Lst}$, $\Omega_{FF_2}^{NLstw}/\omega_0^{st}$ and $\Omega_{BBw}^{NLst}/\omega_0^{Lst}$ for LS-S with and without WEF separately for each stacking sequence as A_{q_1} increases from 0.05 to 0.5 with increments of 0.05. As requested, the main focus is on the role of the WEF effect within SDT, pattern effect, and stacking sequence effect. A common observation for all stacking sequences is that, as A_{q_1} increases, the BB curve exhibits the most regular increase, while FF_1 and FF_2 display a more sensitive transition region at low amplitudes.

When the behavior of spherical shells on WEF is examined in terms of the nonlinear frequency to linear frequency ratio (NLF/LF), it is seen that the layer arrangement has a significant effect on the nonlinear hardening character. In general, in all arrangements, as the dimensionless amplitude increases, the NLF/LF ratios increase, and the systems exhibit nonlinear hardening behavior. However, the magnitude of hardening, the effect of shear deformation, the layer model, and the contribution of a WEF show significant differences depending on the layer arrangement. When the (0°) arrangement is generally considered as the reference structure, the (0°/90°/0°) and (90°/0°/90°) arrangements reveal different nonlinear behavior characteristics. The (0°/90°/0°) arrangement, where the outer layers are oriented at 0°, gives results quite close to the reference (0°) structure in terms of NLF/LF ratios. While the difference between the two structures remains negligible at low amplitudes, as the amplitude increases, the (0°/90°/0°) arrangement systematically lags behind the reference structure. In contrast, the (90°/0°/90°) arrangement with the outer layers oriented at 90° exhibits higher NLF/LF ratios than the reference structure at low amplitudes, but loses this advantage as the amplitude increases, falling below the reference structure at high amplitudes. This indicates that although the (90°/0°/90°) arrangement is initially advantageous, its hardening capacity is more limited at high amplitudes (Figs. 11-13).

There are significant differences between the two configurations in terms of shear deformation effects. In the (0°/90°/0°) configuration, differences reaching 2–3% are observed between the SDT and CST results, especially in the X-model, indicating that shear deformation constitutes a significant and not entirely negligible effect. In contrast, in the (90°/0°/90°) configuration, the SDT and CST results almost coincide, with differences remaining below 1% in most cases. This result shows that structures with outer layers oriented at 90° are much less susceptible to shear deformation (Figs. 12 and 13).

The two configurations also behave differently in terms of layer model effects. In the (0°/90°/0°) configuration, the effect of the O-model is slightly enhancing at low amplitudes, weakening as the amplitude increases, and in some cases becoming negative. The X-model, on the other hand, can exhibit reducing behavior at low amplitudes and enhancing behavior at high amplitudes. Therefore, in this configuration, model effects exhibit a complex character that can change direction depending on the amplitude. In contrast, the effect of the O-model is quite limited in the (90°/0°/90°) configuration, mostly remaining close to zero. The X-model, on the other hand, reduces the NLF/LF ratios slightly but systematically throughout the amplitude range. Therefore, the (0°/90°/0°) configuration is the most sensitive to model changes, while the (90°/0°/90°) configuration shows more stable behavior (Figs. 12 and 13).

The effect of a WEF increases the NLF/LF ratios in both configurations; however, the magnitude of this increase differs. While the soil contribution generally remains at the level of 1–3% in the (0°/90°/0°) configuration, this contribution reaches the range of 4–7% in the (90°/0°/90°) configuration. It is observed that the soil effect becomes even more pronounced as the amplitude increases, especially in the O and U models. This situation shows that the nonlinear hardening behavior of structures with a 90° outer layer benefits more from soil support. In other words, Winkler substrates not only provide additional rigidity but also increase the rate of development of the nonlinear hardening curve (Figs. 11-13).

5.3.3. Comparative analysis of SDT and CST for the nonlinear forced vibrations of laminated nanocomposite shallow hypar shells on a WEF

Tables 3 and 4 present the behavior of $\Omega_{FF_1}^{NLstw}$, $\Omega_{FF_2}^{NLstw}$ and Ω_{BB}^{NLstw} for LHP-S with and without a WEF as A_{q_1} increases from 0.05 to 0.5 with increments of 0.05. The NL dynamic behavior of the hypar shell resting on a WEF is systematically investigated in terms of forced frequencies (FF_1 and FF_2) and the nonlinear BB frequency for different stacking sequences and material distribution patterns (U, O, X). The obtained results clearly demonstrate that the dynamic response of the system is governed by the combined effects of foundation stiffness, stacking sequence, and material distribution pattern. For all configurations, as the amplitude parameter A_{q_1} increases from 0.05 to 0.5, the FF_1, FF_2 and BB frequency values increase monotonically. With increasing amplitude, geometric NL effects enhance the effective stiffness of the structure. In contrast, the discrepancy between SDT and CST decreases with increasing amplitude, indicating that the relative importance of shear deformation diminishes at higher amplitudes.

(0°/90°/0°) Stacking Sequence: All frequency parameters exhibit a regular increase with increasing A_{q_1}, indicating a stable NL hardening behavior. In this configuration, the effect of shear deformation is particularly pronounced for O- and X- patterns. At low amplitudes, the difference between SDT and classical theory reaches approximately 55–58%, whereas at higher amplitudes it decreases to the range of 38–52%. This reduction suggests that geometric nonlinearities suppress shear effects at higher amplitudes. Compared to U-pattern, the O-pattern reduces the frequencies by approximately 14–27%, thus introducing a softening effect, whereas the X-pattern increases the frequencies by about 10–21%, resulting in the stiffest dynamic response. Accordingly, the overall ranking for this configuration is: X>U>O. When compared with the (0°) reference case, this configuration produces very similar results for U-model, a slight reduction for O-model, and a limited increase for X-model in

certain frequency components. This indicates that the fundamental stiffness characteristics of the system are largely preserved. The WEF increases the frequencies for this configuration. The forced frequencies increase by approximately 2–4%, while the BB frequency shows a more limited increase, around 1%, particularly for the X-pattern. This indicates that the foundation effect is more pronounced in the forced dynamic response than in the BB behavior.

(90°/0°/90°) Stacking Sequence: This configuration produces the lowest frequency values among all cases. The 90°orientation in the outer layers significantly reduces the overall stiffness of the structure. Even at high amplitudes, the frequency levels remain considerably lower than those of other configurations. In this case, the effect of shear deformation (SD) is relatively small, with differences generally within the range of 3–7%, indicating that shear deformation does not play a critical role for this configuration. Compared to U-model, the O-model causes a slight reduction in frequency, while the X -model provides a minor positive contribution at low amplitudes but loses this advantage as the amplitude increases, eventually leading to a negative effect. Relative to the (0°) reference, the frequencies in this configuration are significantly reduced, with decreases reaching approximately 30–60% in some cases. This clearly indicates that this stacking sequence is one of the weakest configurations in terms of dynamic performance. However, the effect of the WEF is most pronounced for this configuration, leading to frequency increases of approximately 5–8%. This result demonstrates that more flexible (lower stiffness) structures benefit more significantly from foundation support.

5.3.4. Comparative analysis of SDT and CST for NLF/LF ratio of laminated nanocomposite shallow hypar shells with and without on a WEF

The variations of the NLF/LF ratio corresponding to the FF_1, FF_2 and BB frequency components of LHP-S with and without elastic foundation with respect to the A_{q_1} for different stacking sequences are illustrated in Figs. 14-16. The main focus, as requested, is on the role of the WEF effect within the framework of SDT, pattern effect, and stacking sequence effect. A common trend observed in all stacking sequences is that as A_{q_1} increases, the NLF/LF ratio corresponding to the FF_1, FF_2 and BB frequency components generally increase. However, this increase is not strictly monotonic, especially in the low-amplitude region. The most stable curve is typically the BB, whereas FF_1 is the most sensitive parameter, exhibiting a short transitional behavior at low A_{q_1}. Another crucial point is that the evaluated quantity here is not an absolute frequency but the NLF/LF ratio. Therefore, some configurations that appear weaker in terms of absolute frequency may exhibit stronger NL amplification in terms of ratios. The WEF does not increase these ratios uniformly; in most cases, it provides a more pronounced contribution on the U- and O-model sides, while its effect is more limited on the X-CST side (Figs. 14-16).

When comparing the NLF/LF ratios of the (0°/90°/0°) and (90°/0°/90°) layering configurations, it is observed that nonlinear effects become more pronounced with increasing vibration amplitude in both structures. However, the orientation of the outer layers creates significant differences in the system behavior. While the (0°/90°/0°) configuration exhibits behavior quite close to the (0°) reference structure in terms of NLF/LF ratios, the (90°/0°/90°) configuration reaches higher ratios than the reference case, especially at high amplitudes. This indicates that the structure with 90° oriented outer layers is more sensitive to nonlinear frequency increases, despite having lower rigidity in terms of absolute frequency values (Figs. 14-16).

The effect of shear deformation manifests at different levels in both configurations. In the (0°/90°/0°) configuration, the differences between the SDT and CST results increase with increasing vibration amplitude, reaching levels of 4–5%, especially at high amplitudes. In contrast, in the (90°/0°/90°) arrangement, these differences remain more limited and, in most cases, do not exceed 1–2%. This result reveals that the structure with 90° oriented outer layers exhibits lower susceptibility to shear deformations.

When the effect of material distribution patterns is examined, it is seen that in both arrangements, the O-pattern increases the NLF/LF ratios, while the X-pattern decreases them. However, the magnitude of that effect is much more pronounced in the (90°/0°/90°) arrangement. Especially at high vibration amplitudes, the order becomes O>U>X, and significant decreases in ratios occur in the X-pattern. In contrast, in the (0°/90°/0°) arrangement, pattern effects are more limited, and system behavior remains quite close to reference structure (Figs. 14-16).

The effect of the WEF is positive in both cases, but the level of contribution differs. In the (0°/90°/0°) configuration, the fundamental effect mostly remains in the 2–4% range, while in the (90°/0°/90°) configuration, it reaches 5–8%. Furthermore, in both structures, the fundamental contribution is more pronounced at lower amplitudes and decreases relatively as the amplitude increases. Consequently, when evaluated in terms of NLF/LF ratios, the (90°/0°/90°) configuration exhibits more sensitivity to both nonlinear frequency increase and fundamental effect, while the (0°/90°/0°) configuration shows a more balanced dynamic character closer to the reference structure (Figs. 14-16).

5.3.5 *Comparative investigation of nonlinear dynamic behavior of laminated spherical and hypar shells*

When shallow spherical and hypar shells are evaluated together, in both geometries, the NL FF_1, FF_2 and BB values increase with increasing amplitude parameters, and the systems exhibit stiffening nonlinear behavior. However, in the hypar shell, due to the different curvature characteristics, the effects of layer arrangement and shear strains become more pronounced. In particular, the high differences in SDT-CST in the hypar shell with a (0°/90°/0°) arrangement indicate that shear deformation may be more critical in this geometry compared to the spherical shell. In terms of forced frequencies, the X-model generally gives the highest value and the O-model the lowest values in both shell types. However, the stiffening effect of the X-model is more clearly evident in the hypar shell, while the softening effect of the O-model is also more pronounced. In BB values, the effect of the WEF remains more limited compared to the forced frequencies. In general, the spherical shell exhibits a more balanced and stable frequency distribution, while the hypar shell shows a nonlinear dynamic character that is more sensitive to layer arrangement, model type, and ground effects.

When comparing the NLF/LF behavior of spherical and hypar shells, it is observed that in both geometries, the ratios of FF_1, FF_2 and BB increase with increasing amplitude, and the systems exhibit hardening nonlinear behavior. However, the nonlinear amplification effect is more pronounced in the hypar shell, and especially in the (90°/0°/90°) arrangement, although the absolute frequencies are low, the NLF/LF ratios can exceed those of the reference structure. In the Sphere shell, the same arrangement loses its advantage at high amplitudes and shows a more limited hardening behavior. In terms of shear deformation effect, the hypar shell behaves more sensitively than the spherical shell, especially in the (0°/90°/0°) arrangement. In contrast, in both geometries, the 90° outer layer arrangements are less susceptible to shear deformation. Although the effect of the WEF increases the NLF/LF ratios in both shells, this increase is stronger in the hypar shell and in most cases reaches levels of 6–8%. Consequently, while the spherical shell exhibits more stable and consistent nonlinear behavior, the hypar shell displays stronger nonlinear amplification effects and a ground-sensitive dynamic character.

6. Concluding Remarks

In this study, the NL forced vibration behavior of doubly curved laminated FG-NC shallow shell surfaces with spherical and hypar geometries resting on a WEF is investigated within SDT. This approach strengthens the theoretical foundation of shell analysis and provides a reliable basis for capturing NL behaviors in multilayered nanocomposite systems. In addition, the reduced NL governing equations are analytically solved using the Method of Multiple Time Scales, allowing the systematic derivation of amplitude-dependent vibration characteristics. The main physical contributions of the study are summarized as follows:

a) BB curve most stably represents the nonlinear hardening behavior of the system, while the FF_1 and FF_2 curves exhibited a more sensitive and wavy character, especially at low amplitudes.
b) NLF/LF ratios generally increased in the range of 5–12%, while temporary decreases of 1–3% could occur in low amplitude regions
c) The shear deformation effect is not constant and increases as the vibration amplitude increases; it rises from approximately 1–3% to 2–6% in arrangements with outer layers oriented at 0°, while it mostly remains below 1% in arrangements with outer layers oriented at 90°.
d) The layering arrangement significantly affects not only the frequency levels but also the growth rate and shape of the curves; stronger nonlinear hardening behavior was observed in arrangements with outer layers oriented at 0°, while a lower but more stable increase occurred in arrangements with outer layers oriented at 90°.
e) WEF increases the frequency ratios in all cases, but this effect depends on the layering arrangement; it remains at the level of 1–3% in structures with outer layers oriented at 0°, while it reaches the levels of 4–7% in structures with outer layers oriented at 90°.
f) The effects of material distribution patterns vary depending on the amplitude in the nonlinear region; the O-pattern strengthens in some cases, while the effect of the X-pattern becomes more significantly negative, thus demonstrating that material grading is a dynamic design parameter.
g) The nonlinear forced vibration behavior cannot be explained by a single parameter, and that amplitude, layering arrangement, material distribution, and Winkler elastic basis effects must be evaluated together; in particular, the basis effect becomes one of the dominant mechanisms determining the system behavior in arrangements where the outer layers are oriented at 90°.

From an aerospace engineering perspective, the results obtained in this study are directly relevant to the preliminary design and dynamic evaluation of lightweight curved components operating near resonance conditions. The proposed formulation can be used to determine the layering arrangements and reinforcement distributions that will move the resonance region away from critical operating excitation frequencies, to evaluate the effectiveness of distributed elastic supports, and to identify structural arrangements exhibiting controllable nonlinear stiffening properties. These possibilities are particularly important for spacecraft coatings, satellite reflectors and antenna components, aerodynamic coatings, curved fuselage panels, and other high-performance

structural systems where simultaneous low mass, high rigidity, dimensional accuracy, and vibration resistance are required.

More broadly, the analytical amplitude-frequency relationships obtained in this study can provide a physics-based infrastructure for reduced-order dynamic simulations, resonance tracking, vibration control strategies, and model-based structural condition assessment. The current approach, which reveals how the adaptation of material properties, layering arrangement, elastic support stiffness, and excitation amplitude interact to determine nonlinear resonance, contributes to the development of safer, lighter, and more dynamically reliable aerospace structures.

Author Contributions

Conceptualization, S.Y.; M.A.; methodology, M.A.; S.Y.; software, M.A.; validation, M.A.; formal analysis, M.A.; S.Y.; investigation, M.A.; resources, M.A.; writing—original draft preparation, M.A.; writing—review and editing S.Y., Supervision, S.Y.

Conflict of Interest Statement

The authors declare no conflicts of interest.

Funding

This research received no external funding.

Data Availability Statement

No data was reported in this study.

References

1. Donnell, L.H.: Stability of thin-walled tubes under torsion. NACA Report No. 479 (1933)
2. Ambartsumian, S.A.: Theory of Anisotropic Shells. NASA, Washington, DC (1964)
3. Volmir, A.S.: Non-Linear Dynamics of Plates and Shells (in Russian). Nauka, Moscow (1972)
4. Reddy, J.N.: Mechanics of Laminated Composite Plates and Shells: Theory and Analysis, 2nd edn. CRC Press, New York (2004). https://doi.org/10.1201/b12409
5. Awrejcewicz, J., Krys'ko, V., Vakakis, A.F.: Nonlinear Dynamics of Continuous Elastic Systems. Springer-Verlag, Berlin, Heidelberg (2004)
6. Shen, H.S.: Functionally Graded Materials: Nonlinear Analysis of Plates and Shells. CRC Press, Boca Raton, Florida; 2009.
7. Iijima, S., Ichihashi, T.: Single-shell carbon nanotubes of 1-nm diameter. Nature 363, 603–605 (1993). https://doi.org/10.1038/363603a0
8. Zhong, R., Cong, H.T., Liu, C.: Fabrication of single-walled carbon nanotubes from multi-walled carbon nanotubes and carbon fiber. Carbon 40, 2970–2973 (2002). https://doi.org/10.1016/S0008-6223(02)00285-3
9. Lin, Y., Zhou, B., Fernando, K.A.S., Liu, P., Allard, L.F., Sun, Y.P.: Polymeric carbon nanocomposites from carbon nanotubes functionalized with matrix polymer. Macromolecules 36, 7199–7204 (2003). https://doi.org/10.1021/ma0348876
10. Soni, S.K., Thomas, B., Kar, V.R.: A comprehensive review on CNTs and CNT-reinforced composites: Syntheses, characteristics, and applications. Mater. Today Commun. 25, 101546 (2020). https://doi.org/10.1016/j.mtcomm.2020.101546
11. Socrates, K.P., Vasanthanathan, A.: The perspectives, synthesis, and archives of CNT-based carbon fiber-reinforced composites: A state-of-the-art review. Polym.-Plast. Technol. Mater. 65, 601–618 (2026). https://doi.org/10.1080/25740881.2026.2636583
12. Sharma, S.K., Miladinovic, S., Sharma, L.K., Gajevic, S., Sharma, Y., Sharma, M., Cukic, S., Stojanovic, B.: Graphene/CNT nanocomposites: Processing, properties, and applications. Nanomaterials 16, 100 (2026). https://doi.org/10.3390/nano16020100
13. Liew, K.M., Pan, Z., Zhang, L.W.: The recent progress of functionally graded CNT-reinforced composites and structures. Sci. China Phys. Mech. Astron. 63, 234601 (2020). https://doi.org/10.1007/s11433-019-1457-2
14. Shen, H.S., Chen, X., Guo, L., Wu, L., Huang, X.L.: Nonlinear vibration of FGM doubly curved panels resting on elastic foundations in thermal environments. Aerosp. Sci. Technol. 47, 434–446 (2015). https://doi.org/10.1016/j.ast.2015.10.011
15. Shen, H.S., He, X.Q.: Large-amplitude free vibration of nanotube-reinforced composite doubly curved panels resting on elastic foundations in thermal environments. J. Vib. Control 23, 2672–2689 (2017). https://doi.org/10.1177/1077546315619280
16. Dat, N.D., Khoa, N.D., Nguyen, P.D., Duc, N.D.: An analytical solution for nonlinear dynamic response and vibration of FG-CNT-reinforced nanocomposite elliptical cylindrical shells resting on elastic

foundations. ZAMM J. Appl. Math. Mech. 100, e201800238 (2019). https://doi.org/10.1002/zamm.201800238
17. Avey, M., Sofiyev, A.H., Fantuzzi, N., Kuruoglu, N.: Primary resonance of double-curved nanocomposite systems using improved nonlinear theory and multi-scales method. Int. J. Non-Linear Mech. 137, 103816 (2021). https://doi.org/10.1016/j.ijnonlinmec.2021.103816
18. Khalaf, A.S., Hasan, H.M.: Nonlinear forced vibration of functionally graded hybrid three-phase nanocomposite toroidal shell segments reinforced by carbon nanotubes (CNTs) and graphene nanoplatelets (GPLs). Thin-Walled Struct. 199, 111876 (2024). https://doi.org/10.1016/j.tws.2024.111876
19. Hu, Z.Y., Xu, J., Wang, Z.X., Li, R.: Free vibration of doubly curved panels reinforced by carbon nanotubes: New analytic solutions under non-Levy-type boundary conditions. Appl. Math. Model. 137, 115701 (2025). https://doi.org/10.1016/j.apm.2024.115701
20. Ke, T.V., Minh, P.V., Duc, N.D.: Free and forced vibration analysis of tri-directional functionally graded porous doubly curved nanoshells integrated with magneto-electro-elastic layers. Comput. Struct. 318, 107964 (2025). https://doi.org/10.1016/j.compstruc.2025.107964
21. Sobhy, M.: Nonlinear bending and vibration of FGCNT cylindrical microshells conveying microfluid under a two-dimensional magnetic field. Arch. Civ. Mech. Eng. 25, 174 (2025). https://doi.org/10.1007/s43452-025-01212-8
22. Gawah, Q., Abdullah, M.A., Al-Osta, M.A., Bourada, F., Tounsi, A., Tounsi, A., Yaylacı, M.: Free vibration analysis of nonlinearly dispersed FG-CNTRC beams on Kerr substrate using an improved FSDT. Struct. Eng. Mech. 93, 475–493 (2025). https://doi.org/10.12989/sem.2025.93.6.475
23. Bagheri, H.: Nonlinear thermal stability of functionally graded spherical shells with CNT reinforcement using GDQ and von Kármán nonlinearity. Acta Mech. 237, 1011–1035 (2026). https://doi.org/10.1007/s00707-025-04556-7
24. Jankowski, P., Zur, K.K.: Steady-state vibration of nanocomposite structures with discontinuities. Aerosp. Sci. Technol. 168, 110885 (2026). https://doi.org/10.1016/j.ast.2025.110885
25. Nayfeh, A.H., Mook, D.T.: Nonlinear Oscillations. Wiley, New York (1995). https://doi.org/10.1002/9783527617586
26. Rao, S.S.: Vibration Analysis of Continuous Systems and Nonlinear Oscillations. Wiley, Hoboken (2007)
27. Tornabene, F., Fantuzzi, N., Bacciocchi, M., Viola, E.: Effect of agglomeration on natural frequencies of FG-CNT laminated doubly curved shells. Compos. Part B Eng. 89, 187–218 (2016). https://doi.org/10.1016/j.compositesb.2015.11.016
28. Ye, C., Wang, Y.G.: Nonlinear forced vibration of functionally graded graphene platelet-reinforced metal foam cylindrical shells: Internal resonances. Nonlinear Dyn. 104, 2051–2069 (2021). https://doi.org/10.1007/s11071-021-06401-7
29. Senkoua, Y., Ngak, F.P.E., Meuyou, H.H., Ntamack, G.E.: Numerical investigation of the vibroacoustic behavior of carbon nanotube-reinforced doubly curved multilayer composite shells. Mech. Solids 59, 4003–4026 (2024). https://doi.org/10.1134/S0025654424605093
30. Sofiyev, A.H., Avey, M.: Nonlinear vibration analysis of multilayer nanocomposite cylindrical shells based on an extended shear deformation theory in thermal environments. Math. Methods Appl. Sci. 48, 16327–16344 (2025). https://doi.org/10.1002/mma.70090
31. Ma, J.C., Gao, H.: Free vibration analysis of hybrid laminated thin-walled cylindrical shells containing multilayer FG-CNTRC plies. Acta Mech. 235, 7711–7731 (2025). https://doi.org/10.1007/s00707-024-04082-y
32. Kerr, A.D.: Elastic and viscoelastic foundation models. J. Appl. Mech. 31, 491–498 (1964). https://doi.org/10.1115/1.3629667
33. Ansari, R., Torabi, J., Shojaei, M.F.: Vibrational analysis of functionally graded carbon nanotube-reinforced composite spherical shells resting on elastic foundations using the variational differential quadrature method. Eur. J. Mech. A Solids 60, 166–182 (2016). https://doi.org/10.1016/j.euromechsol.2016.07.003
34. Fan, Y., Xiang, Y., Shen, H.S.: Nonlinear forced vibration of FG-GRC laminated plates resting on visco-Pasternak foundations. Compos. Struct. 209, 443–452 (2019). https://doi.org/10.1016/j.compstruct.2018.10.084
35. Sobhy, M., Zenkour, A.M.: Vibration analysis of functionally graded graphene platelet-reinforced composite double-curved shallow shells on elastic foundations. Steel Compos. Struct. 33, 195–208 (2019). https://doi.org/10.12989/scs.2019.33.2.195
36. Shmatko, T., Kurpa, L., Awrejcewicz, J.: Dynamic analysis of functionally graded sandwich shells resting on elastic foundations. Acta Mech. 233, 1895–1910 (2022). https://doi.org/10.1007/s00707-022-03200-y

37. Eltaher, M.A., Daikh, A.A., Hamdi, A., Abdelhaffez, G.S., Abdraboh, A.M.: Refined nonlocal strain gradient theory for mechanical response of cosine FG-GRNC laminated nanoshells rested on elastic foundation. Adv. Nano Res. 17, 335–350 (2024). https://doi.org/10.12989/anr.2024.17.4.335
38. Awrejcewicz, J., Kudra, G., Mazur, O.: Stability and bifurcation analysis of simply supported rectangular nanoplate embedded on visco-Pasternak foundation based on first-order shear deformation theory. Compos. Struct. 354, 118728 (2025). https://doi.org/10.1016/j.compstruct.2024.118728
39. Li, H., Zhang, W., Zhang, Y.F., Guo, X.: Nonlinear dynamic responses of variable-thickness graphene-reinforced porous aluminum-based sandwich plate with MFC and elastic foundation. Mech. Syst. Signal Process. 242, 113657 (2026). https://doi.org/10.1016/j.ymssp.2025.113657
40. Singha, M.K., Daripa, R.: Nonlinear vibration and dynamic stability analysis of composite plates. J. Sound Vib. 328, 541–554 (2009). https://doi.org/10.1016/j.jsv.2009.08.020
41. Sheng, G.G., Wang, X.: Nonlinear vibrations of FG cylindrical shells subjected to parametric and external excitations. Compos. Struct. 191, 78–88 (2018). https://doi.org/10.1016/j.compstruct.2018.02.018

Appendix A

The linear and nonlinear operators appear in Eqs. (26)–(29) are defined as follows:

$$L_{11}\Phi = h\left[(A_{11}-A_{31})\frac{\partial^4\Phi}{\partial x^2\partial y^2}+A_{12}\frac{\partial^4\Phi}{\partial x^4}\right], L_{12}\Psi_1 = A_{15}\frac{\partial^3\Psi_1}{\partial x^3}+A_{35}\frac{\partial^3\Psi_1}{\partial x\partial y^2}-I_3\frac{\partial\Psi_1}{\partial x}-\rho_2\frac{\partial^3\Psi_1}{\partial x\partial t^2}$$
$$L_{13}\Psi_2 = \left(A_{18}+A_{38}\right)\frac{\partial^3\Psi_2}{\partial x\partial y^2}, L_{14}w = -A_{13}\frac{\partial^4 w}{\partial x^4}-\left(A_{14}+A_{32}\right)\frac{\partial^4 w}{\partial x^2\partial y^2}+\rho_1\frac{\partial^4 w}{\partial x^2\partial t^2} \quad \text{(A1)}$$

$$L_{21}\Phi = h\left[A_{21}\frac{\partial^4\Phi}{\partial y^4}+(A_{22}-A_{31})\frac{\partial^4\Phi}{\partial x^2\partial y^2}\right], L_{22}\Psi_1 = \left(A_{35}+A_{25}\right)\frac{\partial^3\Psi_1}{\partial x\partial y^2}$$
$$L_{23}\Psi_2 = A_{38}\frac{\partial^3\Psi_2}{\partial x^2\partial y}+A_{28}\frac{\partial^3\Psi_2}{\partial y^3}-I_4\frac{\partial\Psi_2}{\partial y}-\rho_3\frac{\partial^3\Psi_2}{\partial y\partial t^2}, L_{24}w = -\left(A_{32}+A_{23}\right)\frac{\partial^4 w}{\partial x^2\partial y^2}-A_{24}\frac{\partial^4 w}{\partial y^4}+\rho_1\frac{\partial^4 w}{\partial x^2\partial t^2} \quad \text{(A2)}$$

$$L_{31}\Phi = -\frac{h}{R_2}\frac{\partial^2\Phi}{\partial x^2}-\frac{h}{R_1}\frac{\partial^2\Phi}{\partial y^2}, L_{32}\Psi_1 = -I_3\frac{\partial\Psi_1}{\partial x}, L_{33}\Psi_2 = -I_4\frac{\partial\Psi_2}{\partial y}$$
$$L_{34}w = \bar{\rho}\frac{\partial^2 w}{\partial t^2}+2\xi\bar{\rho}\frac{\partial w}{\partial t}-K_w w, NL_3\left(\Phi,w\right) = -h\frac{\partial^2\Phi}{\partial y^2}\frac{\partial^2 w}{\partial x^2}+2h\frac{\partial^2\Phi}{\partial x\partial y}\frac{\partial^2 w}{\partial x\partial y}-h\frac{\partial^2\Phi}{\partial x^2}\frac{\partial^2 w}{\partial y^2} \quad \text{(A3)}$$

$$L_{41}\Phi = h\left[B_{11}\frac{\partial^4\Phi}{\partial y^4}+(B_{12}+B_{21}+B_{31})\frac{\partial^2\Phi}{\partial x^2\partial y^2}+B_{22}\frac{\partial^4\Phi}{\partial x^4}\right],$$
$$L_{42}\Psi_1 = B_{25}\frac{\partial^3\Psi_1}{\partial x^3}\left(B_{15}+B_{35}\right)\frac{\partial^3\Psi_1}{\partial x\partial y^2}, L_{43}\Psi_2 = \left(B_{28}+B_{38}\right)\frac{\partial^3\Psi_2}{\partial x^2\partial y}+B_{18}\frac{\partial^3\Psi_2}{\partial y^3},$$
$$L_{44}w = -B_{23}\frac{\partial^4 w}{\partial x^4}+\left(B_{32}-B_{24}-B_{13}\right)\frac{\partial^4 w}{\partial x^2\partial y^2}-B_{14}\frac{\partial^4 w}{\partial y^4}+\frac{1}{R_1}\frac{\partial^2 w}{\partial x^2}+\frac{1}{R_2}\frac{\partial^2 w}{\partial y^2}, \quad \text{(A4)}$$
$$NL_4(w,w) = -\left(\frac{\partial^2 w}{\partial x\partial y}\right)^2+\frac{\partial^2 w}{\partial x^2}\frac{\partial^2 w}{\partial y^2}$$

where B_{ij} and C_{ij} are given as follows:

$$
\begin{aligned}
&B_{11}=\frac{A_{22}^{0}}{A_{00}}, B_{12}=-\frac{A_{12}^{0}}{A_{00}}, B_{13}=\frac{A_{12}^{0}A_{21}^{1}-A_{11}^{1}A_{22}^{0}}{A_{00}}, B_{14}=\frac{A_{12}^{0}A_{22}^{1}-A_{12}^{1}A_{22}^{0}}{A_{00}}, B_{15}=\frac{A_{25}^{0}A_{12}^{0}-A_{15}^{0}A_{22}^{0}}{A_{00}},\\
&B_{18}=\frac{A_{28}^{0}A_{12}^{0}-A_{18}^{0}A_{22}^{0}}{A_{00}}, B_{21}=-\frac{A_{21}^{0}}{A_{00}}, B_{23}=\frac{A_{11}^{1}A_{21}^{0}-A_{21}^{1}A_{11}^{0}}{A_{00}}, B_{22}=\frac{A_{11}^{0}}{A_{00}}, B_{24}=\frac{A_{12}^{1}A_{21}^{0}-A_{22}^{1}A_{11}^{0}}{A_{00}},\\
&B_{25}=\frac{A_{15}^{0}A_{21}^{0}-A_{25}^{0}A_{11}^{0}}{A_{00}}, B_{28}=\frac{A_{18}^{0}A_{21}^{0}-A_{28}^{0}A_{11}^{0}}{A_{00}}, B_{31}=\frac{1}{A_{66}^{0}}, B_{32}=-\frac{2A_{66}^{1}}{A_{66}^{0}}, B_{35}=\frac{A_{35}^{0}}{A_{66}^{0}}, B_{38}=\frac{A_{38}^{0}}{A_{66}^{0}},\\
&A_{00}=A_{11}^{0}A_{22}^{0}-A_{12}^{0}A_{21}^{0}.
\end{aligned}
\tag{A5}
$$

$$
\begin{aligned}
&C_{11}=A_{11}^{1}B_{11}+A_{12}^{1}B_{21}, C_{12}=A_{11}^{1}B_{12}+A_{12}^{1}B_{11}, C_{13}=A_{11}^{1}B_{13}+A_{12}^{1}B_{23}+A_{11}^{2}\ \ C_{14}=A_{11}^{1}B_{14}+A_{12}^{1}B_{24}+A_{12}^{2},\\
&C_{15}=A_{11}^{1}B_{15}+A_{12}^{1}B_{25}+A_{15}^{1}, C_{18}=A_{11}^{1}B_{18}+A_{12}^{1}B_{28}+A_{18}^{1}, C_{21}=A_{21}^{1}B_{11}+A_{22}^{1}B_{21}, C_{22}=A_{21}^{1}B_{12}+A_{22}^{1}B_{22},\\
&C_{23}=A_{21}^{1}B_{13}+A_{22}^{1}B_{23}+A_{21}^{2}, C_{24}=A_{21}^{1}B_{14}+A_{22}^{1}B_{24}+A_{22}^{2}, C_{25}=A_{21}^{1}B_{15}+A_{22}^{1}B_{25}+A_{25}^{1},\\
&C_{28}=A_{21}^{1}B_{18}+A_{22}^{1}B_{28}+A_{28}^{1}, C_{31}=A_{66}^{1}B_{31}, \ \ C_{32}=A_{66}^{1}B_{32}+2A_{66}^{2}, \ \ C_{35}=A_{35}^{1}-A_{66}^{1}B_{35}, C_{38}=A_{38}^{1}-A_{66}^{1}B_{38}
\end{aligned}
\tag{A6}
$$

in which

$$
\begin{aligned}
&A_{ij}^{k_1}=\sum_{k=1}^{N}\int_{z_{k-1}}^{z_k} Y_{ij\bar{z}}^{(k)} z^{k_1}\mathrm{d}z,\ (i,j=1,2,6),\ k_1=0,1,2,\ A_{j5}^{k_2}=\sum_{k=1}^{N}\int_{z_{k-1}}^{z_k} z^{k_2} I_{1z}^{(k)} Y_{1j\bar{z}}^{(k)}\mathrm{d}z, A_{j8}^{k_2}=\sum_{k=1}^{N}\int_{z_{k-1}}^{z_k} z^{k_2} I_{2z}^{(k)} Y_{j2\bar{z}}^{(k)}\mathrm{d}z,\\
&A_{35}^{k_2}=\sum_{k=1}^{N}\int_{z_{k-1}}^{z_k} z^{k_2} I_{1z}^{(k)} Y_{66\bar{z}}^{(k)}\mathrm{d}z, A_{38}^{k_2}=\sum_{k=1}^{N}\int_{z_{k-1}}^{z_k} z^{k_2} I_{2z}^{(k)} Y_{66\bar{z}}^{(k)}\mathrm{d}z,\ k_2=0,1, I_3=\sum_{k=1}^{N}\int_{z_{k-1}}^{z_k}\frac{\mathrm{d}f_1^{(k)}}{\mathrm{d}z}\mathrm{d}z,\ I_4=\sum_{k=1}^{N}\int_{z_{k-1}}^{z_k}\frac{\mathrm{d}f_2^{(k)}}{\mathrm{d}z}\mathrm{d}z.
\end{aligned}
\tag{A7}
$$

Appendix B

1. Mathematical Verification of the Boundary Conditions

The boundary conditions specified in Eq. (30) of the manuscript are as follows.

$w=0,\ M_{11}=0,\ \Psi_2=0$ at $x=0$ and a

$w=0,\ M_{22}=0,\ \Psi_1=0$ at $y=0$ and b

The approximation functions introduced in Eq. (31) are expressed as follows:

$$
w(x,y,t)=W(t)\sin(\bar{m}x)\sin(\bar{n}y),\ \Psi_1(x,y,t)=\Psi_{10}(t)\cos(\bar{m}x)\sin(\bar{n}y),\ \Psi_2(x,y,t)=\Psi_{20}(t)\ \sin(\bar{m}x)\cos(\bar{n}y).
$$

Here, $\bar{m}=m\pi/a$ and $\bar{n}=n\pi/b$ where m and n are positive integers representing the corresponding mode numbers.

A. Verification of the Displacement and Rotational Boundary Conditions

For $x=0$ and $x=a$: $\sin\bar{m}x=0$. Consequently, $w=0,\ \Psi_2=0$

Similarly, for $y=0$ and $y=b$: $\sin\bar{n}y=0$. Therefore, $w=0,\ \Psi_1=0$

Thus, these four boundary conditions are directly satisfied by the adopted approximation functions.

B. Verification of the Bending Moment Boundary Conditions

This is the main issue raised by the reviewer.

Using Eqs. (14), (16), and (18) of the manuscript, the bending moments can be expressed in the following general form:

$$M_{11} = c_{11}T_{11} + c_{12}T_{22} - c_{13}\frac{\partial^2 w}{\partial x^2} - c_{14}\frac{\partial^2 w}{\partial y^2} + c_{15}\frac{\partial \phi}{\partial x} + c_{18}\frac{\partial \psi}{\partial y}$$

$$M_{22} = c_{21}T_{11} + c_{22}T_{22} - c_{23}\frac{\partial^2 w}{\partial x^2} - c_{24}\frac{\partial^2 w}{\partial y^2} + c_{25}\frac{\partial \phi}{\partial x} + c_{28}\frac{\partial \psi}{\partial y}$$

Here, the coefficients c_{ij} are given explicitly in Appendix A, as defined in Eq. (A6).

$C_{11} = A_{11}^{1}B_{11} + A_{12}^{1}B_{21},\ C_{12} = A_{11}^{1}B_{12} + A_{12}^{1}B_{11},\ C_{21} = A_{21}^{1}B_{11} + A_{22}^{1}B_{21},\ C_{22} = A_{21}^{1}B_{12} + A_{22}^{1}B_{22},$

in which the coefficients $A_{ij}^{k_1}$ are defined in Appendix A, as given in Eq. (A7).

Substitution of the approximation functions

Substituting Eq. (31), we obtain:

$$\frac{\partial^2 w}{\partial x^2} = -\bar{m}^2 W(t)\sin(\bar{m}x)\sin(\bar{n}y)\ ,\ \frac{\partial^2 w}{\partial y^2} = -\bar{n}^2 W(t)\sin(\bar{m}x)\sin(\bar{n}y)$$

Furthermore,

$$\frac{\partial \Psi_1}{\partial x} = -\bar{m}\Psi_{10}(t)\sin(\bar{m}x)\sin(\bar{n}y),\ \frac{\partial \Psi_1}{\partial x} = -\bar{n}\Psi_{10}(t)\sin(\bar{m}x)\sin(\bar{n}y)$$

It is evident that all four expressions contain the common factor: $\sin(\bar{m}x)\sin(\bar{n}y)$

Consequently, these terms vanish along the corresponding boundaries.

However, the membrane–bending coupling terms appearing in the bending moment expressions must be examined separately.

For laminated structural elements composed of cross-ply layers, the membrane–bending coupling coefficients $C_{11}, C_{12}, C_{21}, C_{22}$ are theoretically zero or numerically negligible. Accordingly,

$C_{11} = C_{12} = C_{21} = C_{22} \approx 0$.

Under this condition, only the previously evaluated trigonometric terms remain in the bending- moment expressions. Since these terms vanish at the corresponding simply supported edges, the following conditions are satisfied. Therefore, $M_{11}(0,y) = M_{11}(a,y) = 0$, and $M_{22}(x,0) = M_{22}(x,b) = 0$.

This result is further verified by numerical calculations performed in Maple for the composite and nanocomposite doubly curved shells considered in this study. All relevant cases are tested for different geometric dimensions and parameters of the cross-ply laminated doubly curved shells. As an illustrative example, the values of the coefficients $C_{11}, C_{12}, C_{21}, C_{22}$ obtained for laminated nanocomposite hyperbolic paraboloid shells with ($h = 0.002\text{m},\ a = 20h,\ b = 2a,\ R_2 = 1.5a,\ R_1 = (-1)R_2,\ T_0 = 300\text{K}$ are presented below. The material properties used in the calculations are given in Subsection 5.1. For the U-, O-and X-patterns, the absolute values of $C_{11}, C_{12}, C_{21}, C_{22}$ remain extremely small and are therefore negligible within the adopted numerical precision. For example, for the U-pattern, $C_{21} = -9.665990\times10^{-12}$ and $C_{22} = 5.091350\times10^{-10}$, while for the O-pattern, $C_{21} = 2.486\times10^{-10}$ and $C_{21} = -6.928\times10^{-9}$. The coefficients C_{11} and C_{12} are obtained as 0.000000 within the adopted numerical precision. For the X-pattern, all four coefficients are obtained as 0.000000. Thus, in all investigated cases, the largest absolute value remains below the order of 10^{-8}, indicating that these terms are numerically negligible.

These very small residual values should be interpreted within the numerical precision of the calculations and floating-point arithmetic; from the viewpoint of the physical and mathematical model, the

contribution of the corresponding coupling terms is negligible. In addition, it has been shown above that the remaining boundary terms vanish mathematically because the selected approximation functions are zero at the corresponding edges. Taking together, these results demonstrate that the adopted approximation functions are consistent with the prescribed boundary conditions and that the boundary conditions are satisfied within numerical precision.

Appendix C

The coefficients U_{ij} involved in (37) and (38) are explicitly expressed as follows.

$$
\begin{aligned}
&U_{11}=\bar{m}^2\left\{e_{30}\left[(A_{11}-A_{31})\bar{n}^2+A_{12}\bar{m}^2\right]-A_{13}\bar{m}^2-\left(A_{14}+A_{32}\right)\bar{n}^2\right\}, U_{12}=\bar{m}\left(A_{15}\bar{m}^2+A_{35}\bar{n}^2+I_3\right),\\
&U_{13}=(A_{18}+A_{38})\bar{m}^2\bar{n}, U_{21}=\bar{n}^2\left\{e_{30}\left[A_{21}\bar{n}^2+(A_{22}-A_{31})\bar{m}^2\right]-\left(A_{32}+A_{23}\right)\bar{m}^2-A_{24}\bar{n}^2\right\},\\
&U_{22}=(A_{25}+A_{35})\bar{m}\bar{n}^2,\ U_{23}=m_2\left(A_{28}\bar{n}^2+A_{38}\bar{m}^2+I_4\right), U_{31}^{w}=e_{30}\left(\frac{\bar{m}^2}{R_2}+\frac{\bar{n}^2}{R_1}\right)-K_w,\\
&U_{32}=2\bar{m}^2\bar{n}^2\left(e_{10}+e_{20}\right), U_{33}=I_3\bar{m}, U_{34}=I_4\bar{n}, U_{11}^{\rho}=-\rho_1\bar{m}^2,\ U_{12}^{\rho}=\rho_2\bar{m}, U_{21}^{\rho}=-\rho_1\bar{n}^2,\ U_{23}^{\rho}=\rho_3\bar{n},\\
&U_{11}^{nl}=\frac{64e_{10}A_{12}}{3ab}\frac{\bar{m}^3}{\bar{n}}\Gamma, U_{21}^{nl}=\frac{64e_{20}A_{21}}{3ab}\frac{\bar{n}^3}{\bar{m}}\Gamma,\ U_{31}^{NL}=\frac{16}{3ab}\left[\frac{e_{10}}{R_2}\frac{\bar{m}}{\bar{n}}+\frac{e_{20}}{R_1}\frac{\bar{n}}{\bar{m}}+\frac{\bar{m}\bar{n}e_{30}}{2}\right]\Gamma.
\end{aligned}
\tag{B1}
$$

The following definitions are used for the symbols appearing in these expressions:

$$
\begin{aligned}
&e_{10}=\frac{1}{32B_{22}}\frac{\bar{n}^2}{\bar{m}^2},\ e_{20}=\frac{1}{32B_{11}}\frac{\bar{m}}{\bar{n}^2},\ \ e_{30}=\frac{\mu_1}{B_{11}\bar{m}^4+(B_{12}+B_{21}+B_{31})\bar{m}^2\bar{n}^2+B_{22}\bar{n}^4},\\
&\Gamma=(-1)^m\left[1+(-1)^{n-m}-(-1)^n-(-1)^{-m}\right]
\end{aligned}
\tag{B2}
$$

TABLE AND FIGURE CAPTIONS

Fig. 1. (a) Geometry of the doubly curved multilayer shell on a WEF, and **(b)** cross-sectional representation of the layered structure.

Fig. 2. Through-thickness distributions of CNT volume fraction in the k^{th} layer of a doubly curved laminated nanocomposite shell surface: U-, O-, and X-type patterns.

Fig. 3. Laminated FG-NC **(a)** spherical and **(b)** hypar shell surfaces on a WEF and the coordinate system.

Fig. 4. Cross-section of doubly curved multilayered FG-NC orthotropic shell surfaces.

Fig. 5. Variation of the nonlinear BB/FF_1/ FF_2 values of the U-, O-, and X-modeled (0°) single-layer spherical shell on a WEF with respect to A_{q_1} within **(a)** SDT and **(b)** CST.

Fig. 6. Variation of the nonlinear BB/FF_1/ FF_2 values of the U-, O-, and X-modeled (0°) single-layer unconstrained spherical shell respect to A_{q_1} within **(a)** SDT and **(b)** CST.

Fig. 7. Variation of the nonlinear BB/FF_1/FF_2 values of the U-, O-, and X-modeled spherical shell with a (0°/90°/0°) layup on a WEF with respect to A_{q_1} within **(a)** SDT and **(b)** CST.

Fig. 8. Variation of the nonlinear BB/FF_1/ FF_2 values of the U-, O-, and X-modeled unconstrained spherical shell with a (0°/90°/0°) layup with respect to A_{q_1} within **(a)** SDT and **(b)** CST.

Fig. 9. Variation of the nonlinear BB/FF_1/FF_2 values of the U-, O-, and X-modeled spherical shell with a (90°/0°/90°) layup on a WEF with respect to A_{q_1} within **(a)** SDT and **(b)** CST.

Fig. 10. Variation of the nonlinear BB/FF_1/ FF_2 values of the U-, O-, and X-modeled unconstrained spherical shell with a (90°/0°/90°) layup with respect to A_{q_1} within **(a)** SDT and **(b)** CST.

Fig. 11. Dependence of the NLF/LF ratios of the U-modeled spherical shells with (0°), (0°/90°/0°), and (90°/0°/90°) layup on the A_{q_1}: for grounded and ungrounded cases within **(a)** SDT and **(b)** CST.

Fig. 12. Dependence of the NLF/LF ratios of the O-modeled spherical shells with (0°), (0°/90°/0°), and (90°/0°/90°) layup on the A_{q_1}: for grounded and ungrounded cases within **(a)** SDT and **(b)** CST.

Fig. 13. Dependence of the NLF/LF ratios of the X-modeled spherical shells with (0°), (0°/90°/0°), and (90°/0°/90°) layup on the A_{q_1}: for grounded and ungrounded cases within **(a)** SDT and **(b)** CST.

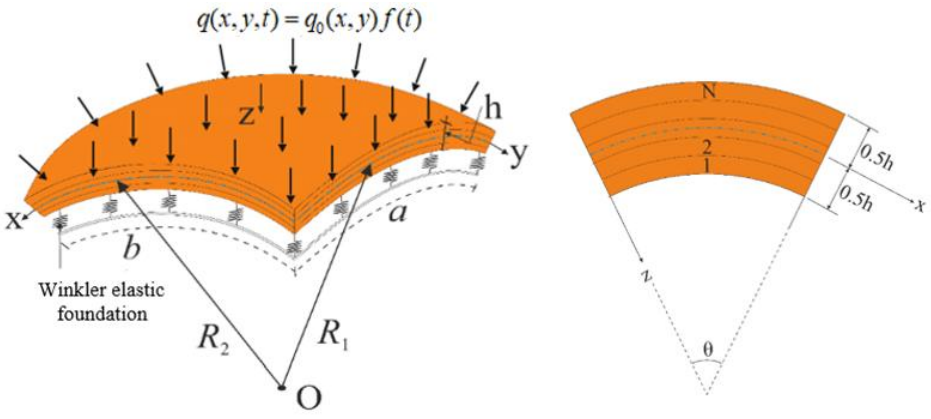
Fig. 14. Dependence of the NLF/LF ratios of the U-modeled hypar shells with (0°), (0°/90°/0°), and (90°/0°/90°) layup on the A_{q_1} : for grounded and ungrounded cases within **(a)** SDT and **(b)** CST.

Fig. 15. Dependence of the NLF/LF ratios of the O-modeled hypar shells with (0°), (0°/90°/0°), and (90°/0°/90°) layup on the A_{q_1} : for grounded and ungrounded cases within **(a)** SDT and **(b)** CST.

Fig. 16. Dependence of the NLF/LF ratios of the X-modeled hypar shells with (0°), (0°/90°/0°), and (90°/0°/90°) layup on the A_{q_1} : for grounded and ungrounded cases within **(a)** SDT and **(b)** CST.

Table 1. Comparison of NLF/LF ratios with the results of Refs. [4] and [25].
Table 2. Comparison of NLF/LF ratios for square single-layer (0°) and cross-ply (0°/90°/0°/90°/0°) homogeneous plates with free boundary conditions.
Table 3. Variation of the nonlinear FF_1, FF_2 and BB frequencies of hypar shells on a WEF with respect to A_{q_1} for different stacking sequences.
Table 4. Variation of the NL FF_1, FF_2 and BB frequencies of unconstrained hypar shells with respect to A_{q_1} for different stacking sequences.

FIGURE 1



(a) **(b)**

FIGURE 2

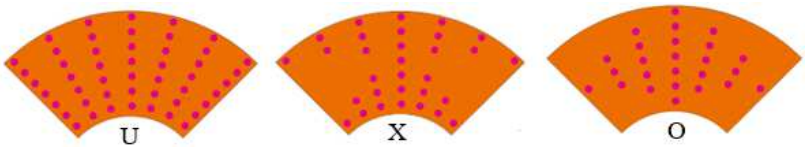
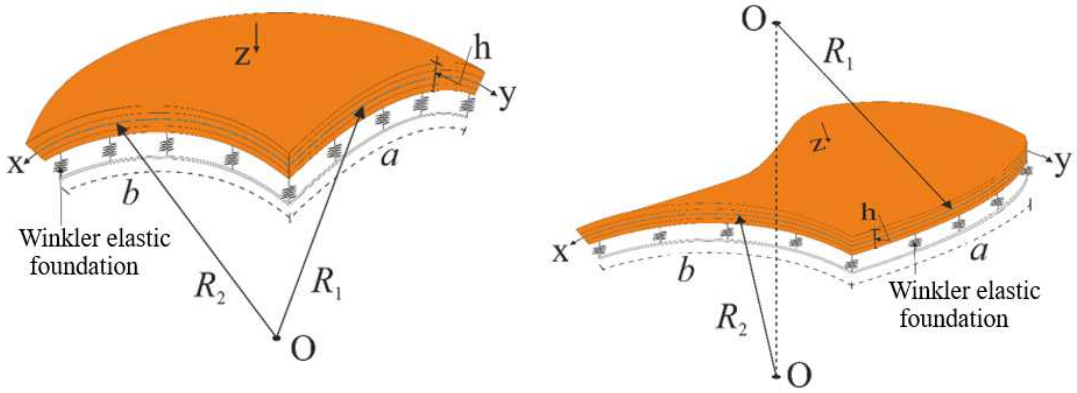


FIGURE 3



(a) **(b)**

FIGURE 4

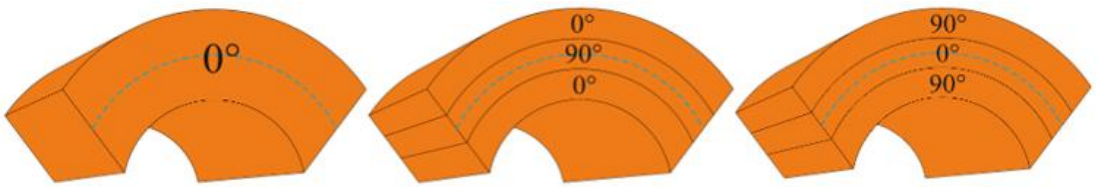
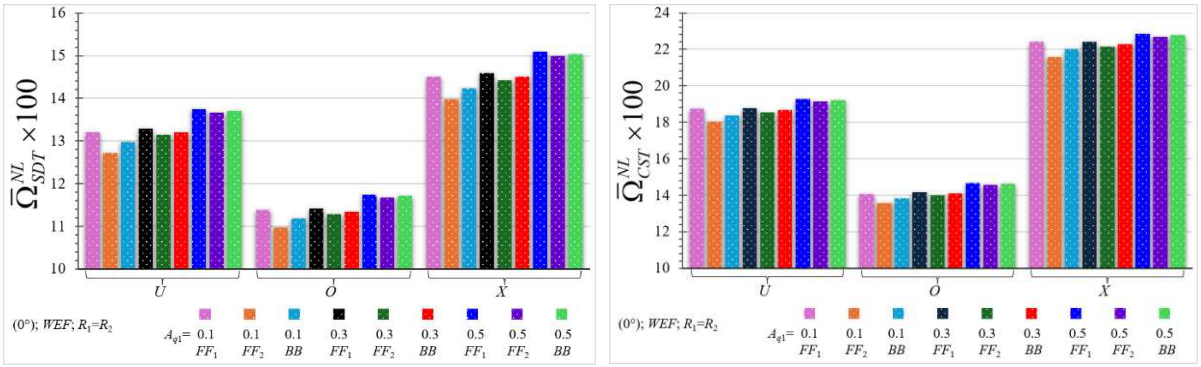
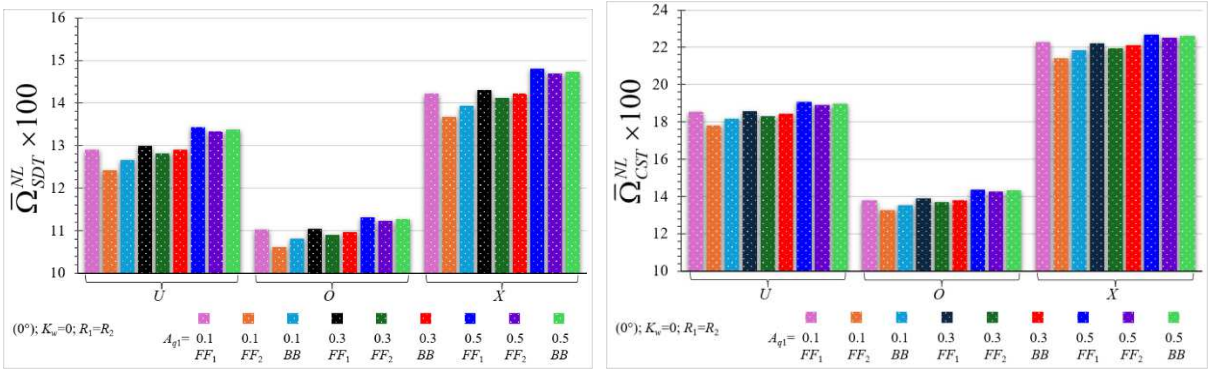


FIGURE 5



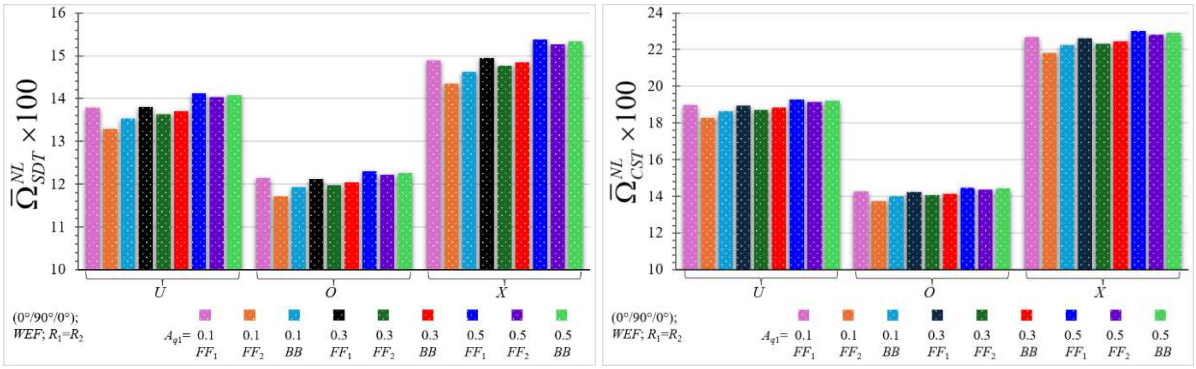
(a) **(b)**

FIGURE 6



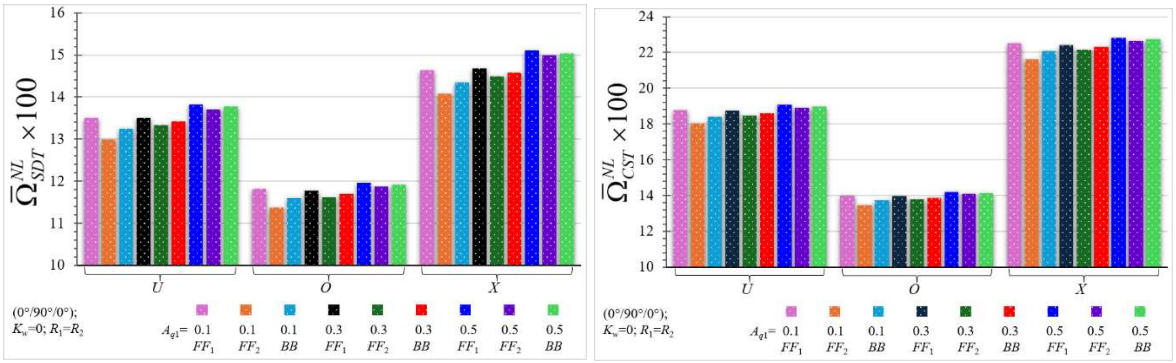
(a) **(b)**

FIGURE 7



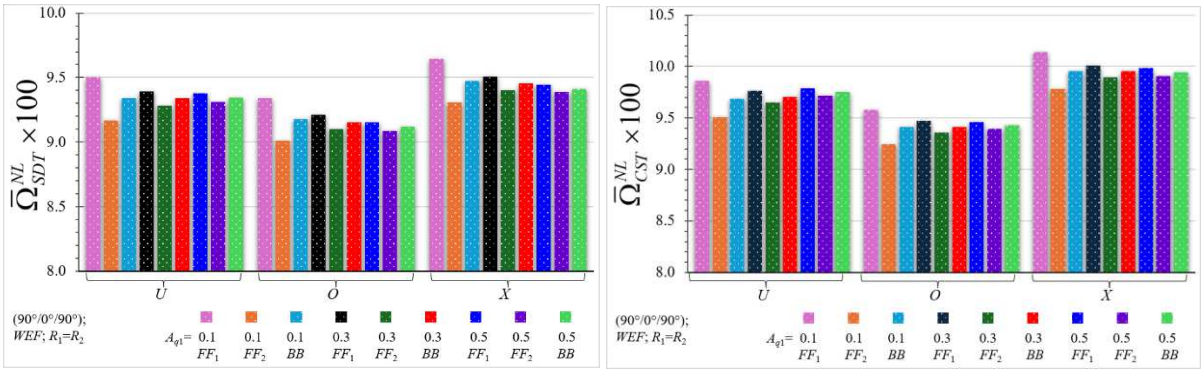
(a) **(b)**

FIGURE 8



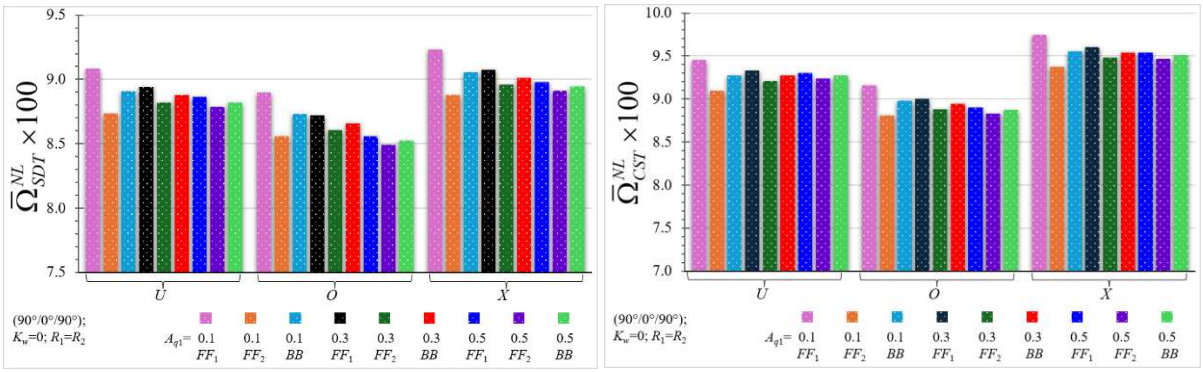
(a) **(b)**

FIGURE 9



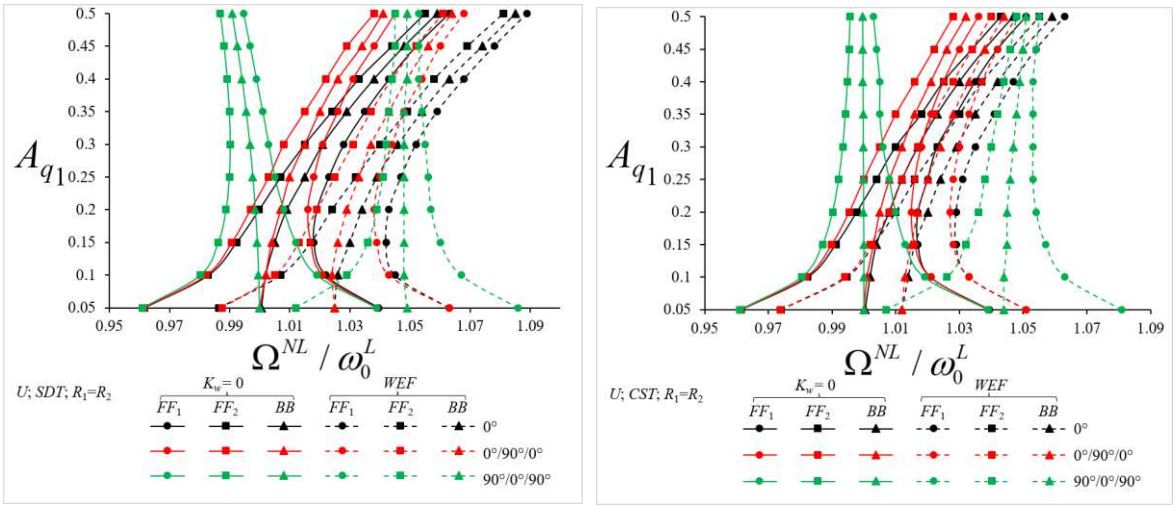
(a) **(b)**

FIGURE 10



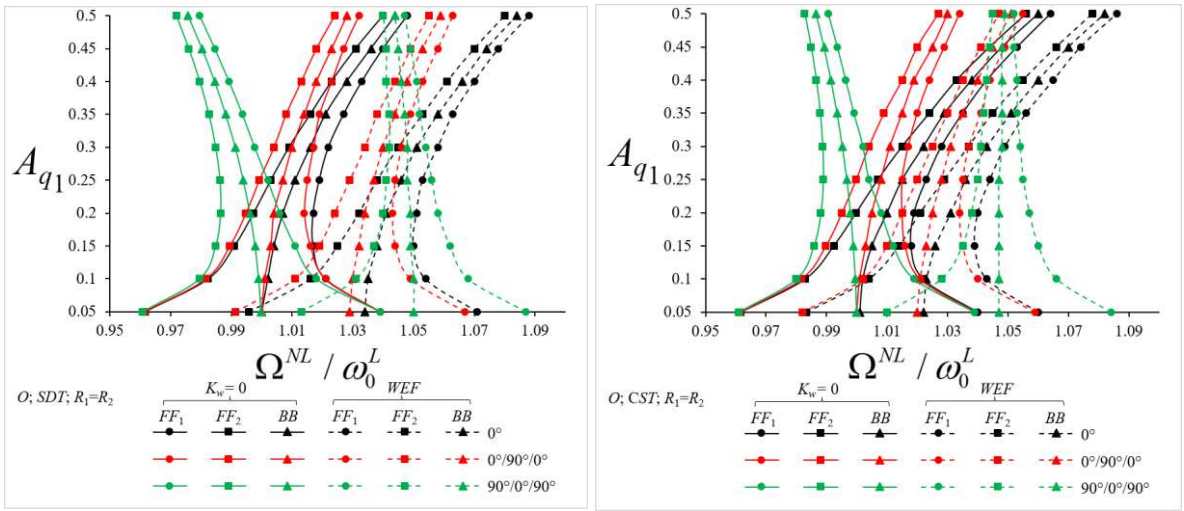
(a) **(b)**

FIGURE 11



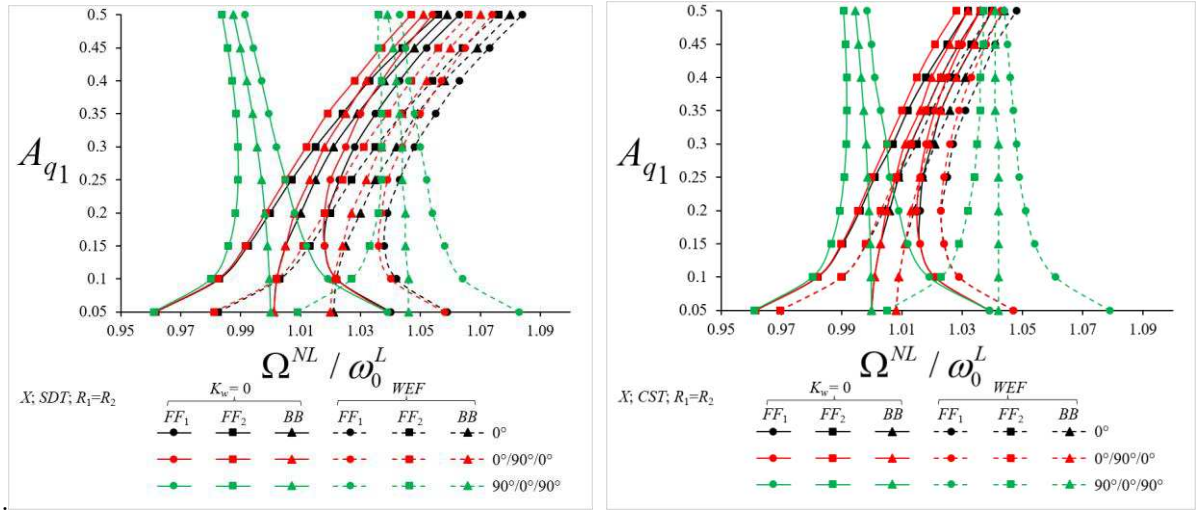
(a) **(b)**

FIGURE 12



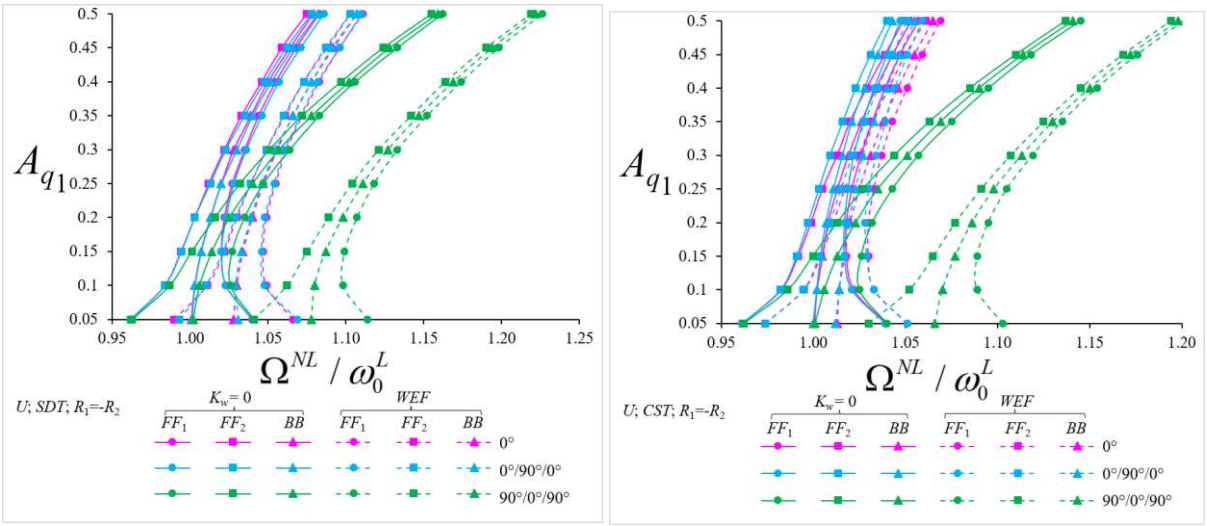
(a) **(b)**

FIGURE 13



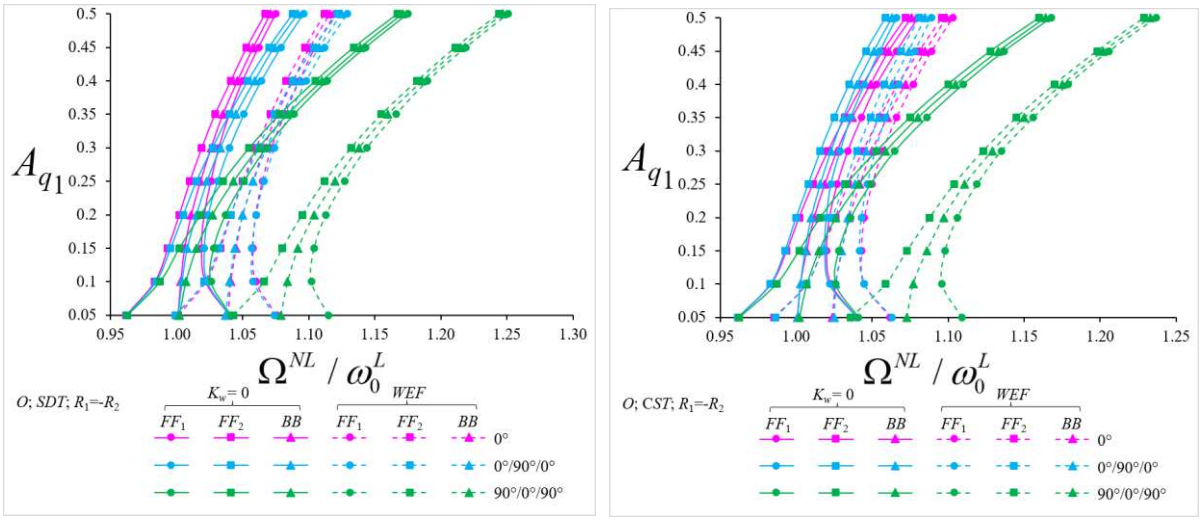
(a) **(b)**

FIGURE 14



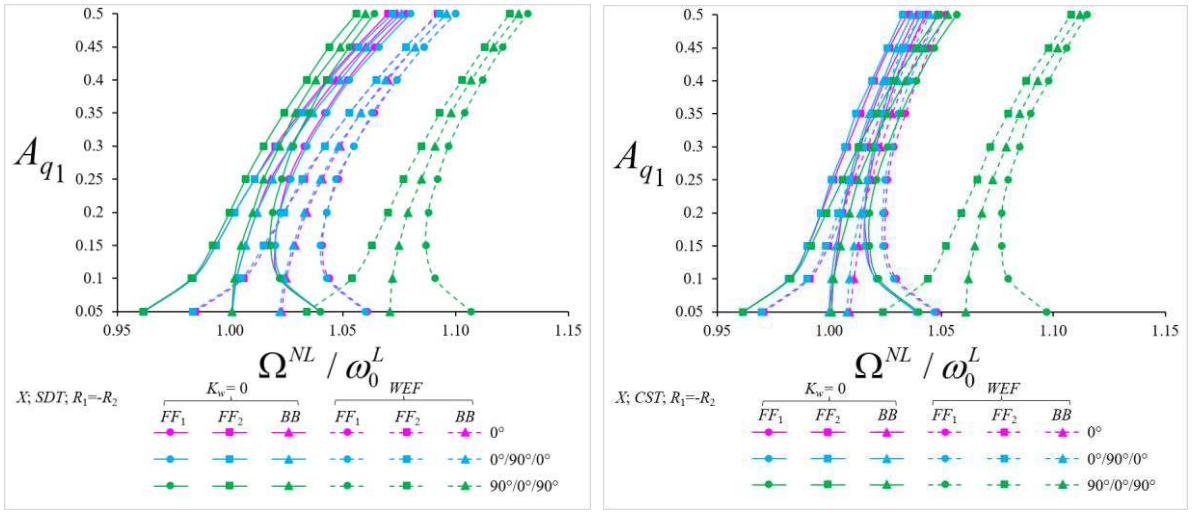
(a) **(b)**

FIGURE 15



(a) **(b)**

FIGURE 16



(a) **(b)**

TABLE 1

A_{q_1} Amplitude	Present study	Nayfeh & Mook [25]	Reddy [4]	Maximum Difference (%)
0.5	1.00012	1.00010	1.00011	0.02
1.0	1.00037	1.00035	1.00036	0.02
1.5	1.00101	1.00098	1.00100	0.03
2.0	1.00237	1.00230	1.00234	0.03

TABLE 2

NLF/LF				
	Single-layer orthotropic laminae		(0°/90°/0°/90°/0°)	
A_{q_1}	Present study	Ref. [40]	Present study	Ref. [40]
0.4	1.020	1.020	1.041	1.042
0.8	1.078	1.079	1.154	1.158
1.2	1.168	1.173	1.320	1.331

TABLE 3

Dimensionless NL frequencies for hypar shells on a WEF																		
(0°)																		
	U						O						X					
	SDT			CST			SDT			CST			SDT			CST		
A_{q_1}	FF_1	FF_2	BB	FF_1	FF_2	BB	FF_1	FF_2	BB	FF_1	FF_2	BB	FF_1	FF_2	BB	FF_1	FF_2	BB
0.05	12.84	11.92	12.38	18.65	17.28	17.97	10.86	10.11	10.49	13.75	12.77	13.27	14.19	13.17	13.69	22.50	20.83	21.68
0.1	12.63	12.18	12.40	18.34	17.66	18.00	10.70	10.32	10.51	13.54	13.05	13.29	13.97	13.46	13.71	22.11	21.28	21.69
0.15	12.61	12.30	12.46	18.27	17.81	18.04	10.67	10.42	10.55	13.51	13.18	13.35	13.93	13.59	13.77	22.01	21.46	21.74
0.2	12.63	12.41	12.53	18.28	17.93	18.11	10.70	1.510	10.61	13.54	13.29	13.41	13.96	13.7	13.84	22.00	21.59	21.80
0.5	13.38	13.29	13.33	18.96	18.83	18.89	11.31	11.23	11.27	14.30	14.19	14.24	14.72	14.62	14.66	22.58	22.42	22.50
A_{q_1}	(0° / 90° / 0°)																	
0.05	12.84	11.92	12.38	18.65	17.28	17.97	10.86	10.11	10.49	13.75	12.77	13.27	14.19	13.17	13.69	22.5	20.83	21.68
0.1	12.63	12.18	12.4	18.34	17.66	18.00	10.70	10.32	10.51	13.54	13.05	13.29	13.97	13.46	13.71	22.11	21.28	21.69
0.15	12.61	12.3	12.46	18.27	17.81	18.04	10.67	10.42	10.55	13.51	13.18	13.35	13.93	13.59	13.77	22.01	21.46	21.74
0.2	12.63	12.41	12.53	18.28	17.93	18.11	10.70	10.51	10.61	13.54	13.29	13.41	13.96	13.7	13.84	22.00	21.59	21.80
0.5	13.38	13.29	13.33	18.96	18.83	18.89	11.31	11.23	11.27	14.30	14.19	14.24	14.72	14.62	14.66	22.58	22.42	22.50
A_{q_1}	(90° / 0° / 90°)																	
0.05	7.826	7.318	7.569	8.396	7.840	8.118	7.779	7.270	7.528	8.077	7.548	7.813	8.111	7.575	7.840	8.715	8.132	8.423
0.1	7.860	7.596	7.725	8.288	8.010	8.145	7.684	7.433	7.562	7.982	7.718	7.847	7.989	7.725	7.854	8.579	8.288	8.430
0.15	7.867	7.698	7.779	8.288	8.104	8.199	7.704	7.535	7.623	7.996	7.820	7.908	7.969	7.786	7.874	8.552	8.355	8.450
0.2	7.921	7.793	7.854	8.335	8.199	8.267	7.765	7.643	7.704	8.057	7.921	7.989	7.976	7.840	7.908	8.552	8.410	8.484
0.5	8.776	8.722	8.749	9.142	9.088	9.115	8.728	8.674	8.701	9.006	8.952	8.979	8.288	8.240	8.260	8.857	8.796	8.823

TABLE 4

Dimensionless NL frequencies for unconstrained hypar shells ($K_w = 0$)																		
(0°)																		
	U						O						X					
	SDT			CST			SDT			CST			SDT			CST		
A_{q_1}	FF_1	FF_2	BB	FF_1	FF_2	BB	FF_1	FF_2	BB	FF_1	FF_2	BB	FF_1	FF_2	BB	FF_1	FF_2	BB
0.05	12.53	11.59	12.06	18.43	17.05	17.74	10.5	9.712	10.11	13.47	12.46	12.97	13.92	12.87	13.39	22.31	20.64	21.49
0.1	12.32	11.85	12.09	18.12	17.43	17.78	10.32	9.929	10.13	13.25	12.74	12.99	13.69	13.16	13.42	21.92	21.09	21.50
0.15	12.29	11.98	12.13	18.05	17.59	17.82	10.30	10.03	10.17	13.21	12.88	13.04	13.65	13.30	13.48	21.82	21.27	21.55
0.2	12.32	12.09	12.20	18.07	17.71	17.89	10.32	10.12	10.21	13.24	12.99	13.12	13.67	13.41	13.54	21.81	21.40	21.61
0.5	13.04	12.95	12.99	18.75	18.61	18.68	10.86	10.78	10.82	13.98	13.89	13.94	14.43	14.32	14.38	22.39	22.23	22.31
A_{q_1}	(0° / 90° / 0°)																	
0.05	12.79	11.83	12.31	18.34	16.96	17.65	10.72	9.915	10.32	13.16	12.17	12.67	13.98	12.94	13.46	22.33	20.66	21.50
0.1	12.44	11.96	12.20	18.03	17.33	17.67	10.55	10.15	10.34	12.94	12.44	12.69	13.75	13.23	13.49	21.93	21.09	21.51
0.15	12.40	12.09	12.25	17.95	17.48	17.71	10.53	10.26	10.39	12.89	12.57	12.73	13.71	13.37	13.54	21.84	21.28	21.55
0.2	12.44	12.2	12.32	17.95	17.59	17.77	10.56	10.36	10.46	12.91	12.66	12.78	13.74	13.48	13.62	21.82	21.4	21.61
0.5	13.2	13.11	13.16	18.49	18.34	18.42	11.29	11.22	11.26	13.5	13.4	13.45	14.53	14.42	14.47	22.35	22.19	22.27
A_{q_1}	(90° / 0° / 90°)																	
0.05	7.471	6.911	7.191	7.916	7.323	7.620	7.257	6.714	6.985	7.575	7.013	7.297	7.616	7.046	7.331	8.254	7.637	7.942
0.1	7.345	7.067	7.202	7.799	7.508	7.657	7.155	6.884	7.019	7.474	7.189	7.331	7.487	7.202	7.345	8.111	7.799	7.955
0.15	7.352	7.169	7.264	7.806	7.609	7.704	7.175	6.992	7.080	7.487	7.297	7.392	7.460	7.270	7.365	8.077	7.874	7.976
0.2	7.413	7.270	7.338	7.854	7.711	7.786	7.236	7.101	7.169	7.542	7.406	7.474	7.467	7.325	7.392	8.084	7.928	8.010
0.5	8.322	8.267	8.294	8.715	8.654	8.681	8.193	8.145	8.166	8.505	8.450	8.478	7.793	7.738	7.765	8.389	8.328	8.362